Differences in topological progression profile among neurodegenerative diseases from imaging data

Sara Garbarino[1,2,*], Marco Lorenzi[2], Neil P. Oxtoby[1], Elisabeth J. Vinke[3], Razvan V. Marinescu[1], Arman Eshaghi[4], M. Arfan Ikram[3,7], Wiro J. Niessen[7], Olga Ciccarelli[4], Frederik Barkhof [1,5], Jonathan M. Schott[6], Meike W. Vernooij[3,7], Daniel C. Alexander[1], for the Alzheimer's Disease Neuroimaging Initiative

1 Centre for Medical Image Computing, University College London, United Kingdom

2 Université Côte d'Azur, Inria, France

3 Department of Epidemiology, Erasmus Medical Center, the Netherlands

4 Institute of Neurology, University College London, United Kingdom

5 Department of Radiology and Nuclear medicine, VUmc, the Netherlands

6 Dementia Research Centre, Institute of Neurology, University College London, United Kingdom

7 Department of Radiology and Nuclear medicine, Erasmus MC, the Netherlands

Corresponding author: Sara Garbarino; email: sara.garbarino@inria.fr

Abstract

The spatial distribution of atrophy in neurodegenerative diseases suggests that brain connectivity mediates disease propagation. Different descriptors of the connectivity graph potentially relate to different underlying mechanisms of propagation. Previous approaches for evaluating the influence of connectivity on neurodegeneration consider each descriptor in isolation and match predictions against late-stage atrophy patterns. We introduce the notion of a *topological profile* — a characteristic combination of topological descriptors that best describes the propagation of pathology in a particular disease. By drawing on recent advances in disease progression modeling, we estimate topological profiles from the full course of pathology accumulation, at both cohort and individual levels. Experimental results comparing topological profiles for Alzheimer's disease, multiple sclerosis and normal ageing show that topological profiles explain the observed data better than single descriptors. Within each condition, most individual profiles cluster around the cohort-level profile, and individuals whose profiles align more closely with other cohort-level profiles show features of that cohort. The cohort-level profiles suggest new insights into the biological mechanisms underlying pathology propagation in each disease.

Introduction

Evidence from neuroimaging suggests that the progression of brain changes in neurodegenerative diseases may be mediated by brain connectivity. For example, atrophy patterns observed with MRI suggest that different brain regions are systematically and selectively vulnerable to different neurodegenerative diseases, and that these atrophy patterns closely match known connectivity networks [1–5]. The literature includes wide

debate on the potential mechanisms underlying pathogenic protein propagation, on the biology of protein aggregation and propagation, and of selective vulnerability of neurons in neurodegenerative disease; see [6–8] for recent reviews. Uncovering the precise relationship between the topology of brain network connectivity and the pattern of pathology may provide clues to the underlying mechanisms of propagation. Indeed, in Alzheimer's disease (AD), Zhou et al [5] attempt to explain the association between patterns of brain atrophy and connectivity in terms of different topological descriptors: 1) *centrality* – the most active regions or 'hubs' are most vulnerable [9,10]; 2) *segregation* – opposite to 1), the most isolated nodes are most vulnerable [11,12]; 3) *network proximity* – regions connected to disease epicenters are most vulnerable [13–15]; 4) *cortical proximity* – regions spatially-adjacent to disease epicenters are most vulnerable. The authors relate these descriptors to distinct mechanisms of pathology propagation: (1) centrality represents nodal stress, (2) segregation, trophic failure, (3) network proximity, trans-neuronal spread, and (4) cortical proximity represents unguided diffusive propagation. Thus comparing patterns of pathology predicted by these different descriptors with those observed in patient cohorts gives clues to which corresponding mechanisms are at play. Moreover, as reviews [6–8] highlight, the plausibility of those mechanisms extend similarly to the wider range of neurodegenerative conditions.

Previous studies [1,2,4,5,10,16–19] using functional or structural networks have focused on evaluating the ability of each individual topological descriptor above to explain observed patient data with the goal of identifying the single most likely mechanism of disease propagation. More generally, a variety of mathematical models based on dynamical systems modeling [20–26] have been proposed for describing the temporal propagation of pathology mediated by brain networks. They mostly enforce the trans-neuronal spread (or "prion-like") hypothesis of propagation via network proximity. These approaches have important methodological limitations, which should prompt caution in their interpretation. Two key limitations are: i) the approaches do not consider the possibility of multiple concurrent spreading mechanisms; ii) the evaluation of topological descriptors is performed using only cross-sectional data assumed to represent end-stage atrophy patterns.

Regarding limitation (i), multiple distinct mechanisms are likely to contribute in diseases where multiple proteinopathies are at play (such as amyloid and tau in AD; see for example [22,27,28]); in diseases exhibiting highly-variable atrophy patterns (as in multiple sclerosis (MS); see [29]); or in individual cases where multiple pathologies co-exist, as for instance tau accumulation in Parkinson's disease [30,31], or alpha-synuclein or TDP-43 in AD [32–35]. Also, associations between vascular factors and neurodegenerative dementias such as AD are common [36,37], which suggests contributions from multiple underlying mechanisms to the observed pattern of pathology accrual [35]. Further, in MS, retrograde neurodegeneration secondary to focal damage from remote lesions, iron accumulation in the deep gray matter and "virtual hypoxia" in the hub regions could all potentially combine and contribute to explain observed neurodegeneration [38].

Regarding limitation (ii), considering only end-stage pathology severely limits sensitivity — like trying to guess the plot of a movie after watching only the final scene [39]. The emergence of data-driven disease progression models (DPMs) [39–54] provides an opportunity to address limitation (ii) by using the full trajectory of pathology accumulation to evaluate the influence of topological descriptors. These techniques estimate the long-term temporal pattern of disease progression directly from cross-sectional or short-term longitudinal data sets on the assumption of some degree of commonality of progression over a patient cohort. In contrast to brute-force machine-learning approaches [56–58] to predict progression, DPMs reveal the trajectory of temporal evolution of multiple biomarkers on a common timeline, which can, in turn, provide an extra dimension for identifying informative topological descriptors over and above using late-stage information alone.

In this paper we set out to ameliorate the aforementioned limitations in network-based models of neurodegenerative disease by revealing the combinations of topological descriptors that best explain the temporal evolution of pathology. We introduce a new method that uses the Gaussian Process (GP)

82　Progression Model of [59] to assess candidate descriptors against the full time course of the disease, rather than
83　just late-stage pathology. Moreover, the method identifies a characteristic combination for each disease that
84　defines a novel disease-specific *topological profile*. We extend this concept further to find personalized
85　topological profiles for each individual and demonstrate the consistency of individual profiles with the
86　corresponding cohort profile as well as characterize within-disease variability of individual topological
87　profiles. We focus on patterns and trajectories of atrophy accumulation informed by structural MRI and use
88　three distinct data sets across the spectrum of neurodegeneration (Alzheimer's disease – AD, primary
89　progressive multiple sclerosis – PPMS, and broadly-healthy ageing represented by data collected from
90　community-dwelling ageing individuals – HA). We show that: a) a combination of topological descriptors
91　consistently explains the data better than the best single descriptor; b) the profiles differ substantially among
92　conditions; c) individual profiles cluster around corresponding cohort-level profiles, but only when the
93　profile is estimated from the full time course rather than end-stage only; and d) positioning of individual
94　profiles with respect to each cohort profile is associated with relevant clinical features, thereby potentially
95　benefiting early diagnosis and stratification.

Results

97　Figure 1 gives an overview of the methods used to compute topological profiles at both cohort and individual
98　levels: full details are provided in the Methods section. In this section we show first that the GP Progression
99　Model estimates trajectories of atrophy evolution that reflect observed atrophy patterns in each cohort (AD,
100　PPMS and HA). Secondly, we show that the topological profiles derived from such atrophy evolution
101　patterns are distinct for each condition and explain observations better than profiles estimated when using
102　end-stage data only, and better than single topological descriptors. Further, we demonstrate that most
103　individual profiles reflect their corresponding cohort profile (and neurological condition), and that those that
104　do not ("outliers") show clinical characteristics of the topologically-nearest cohort.

Temporal patterns estimated by the GP Progression Model confirm observed atrophy progression patterns

106　Figure 2, top row, shows the spatio-temporal evolution of the atrophy patterns in each cohort (AD, PPMS
107　and HA) estimated by the GP Progression Model over 41 bilateral regions of interest, obtained by
108　symmetrizing the 82 anatomical regions from the segmentation procedure in [60] (see Methods: Data
109　description). Each panel shows four temporal stages sampled at uniform intervals according to the estimated
110　disease time of the GP Progression Model (see Methods: GP Progression Model). Each topological profile
111　specifies the rate of pathology accumulation in each area. So, while the rates are time-independent, they vary
112　spatially so that the pattern itself is time dependent. Figure 2–figure supplement 1 shows a higher temporal
113　resolution visualization of the same progressions. The regional trajectories and the individual time
114　parameters estimated by the model are shown in Figure 2-figure supplement 2, Figure 2-figure supplement 3
115　and Figure 2-figure supplement 4.
116　　In the AD cohort, the first regions to show atrophy are the superior temporal region and the
117　hippocampus, followed by the amygdala, the remaining temporal regions, the insular and the supramarginal
118　regions, and then the precentral and postcentral regions and the posterior lobe. The estimated progression
119　gradually involves the occipital lobe, the middle frontal region, and finally the remaining subcortical areas,
120　with thalamus and caudate last, which matches well-known atrophy progression patterns observed in AD
121　from post-mortem histology [61] and in-vivo disease progression models [41,44,55,59]. In PPMS the progression
122　first involves some subcortical areas (caudate, thalamus, pallidum), followed by the superior parietal region,
123　the remaining subcortical areas (amygdala, putamen, nucleus accumbens), few frontal regions (mostly
124　middle- and orbito-frontal), the precentral, and then the occipital and temporal lobes, which become
125　abnormal later in the progression. The dynamics of progression agree with recent results [42,62], obtained using
126　a different DPM. In the HA cohort, we observe early involvement of the insula, the superior and middle
127　temporal lobes, the middle frontal, and the putamen. Subsequently, the amygdala, hippocampus and nucleus

128 accumbens are affected, the inferior temporal and more frontal regions, followed by the parietal lobe and the
129 cingulate. This agrees with other studies of volume loss in normal aging [63,64,65].

Distinct topological profiles for each neurological condition

131 The second row of Figure 2 shows the progression corresponding to the topological profiles that best match
132 the GP Progression Model, for each cohort. The topological profiles are sparse linear combinations of nine
133 network metrics, each representing one of five topological descriptors. They are the four described in [5] –
134 centrality, segregation, network proximity and cortical proximity – and the constant progression descriptor,
135 quantifying the extent to which the rate of atrophy remains constant throughout the progression (see
136 Methods: Network metrics). Table 1 shows the weight of each metric in the profile for each condition that
137 best explains the corresponding GP disease progression in Figure 2 top row. Weights with value below 0.10
138 are set to zero in the final sparse linear combination defining the topological profiles; those weights are
139 shown in bold in Table 1.

140 Table 1 shows that the topological profiles for AD, PPMS and HA differ substantially. Specifically, AD
141 shows a concurrency of centrality metrics (40%) and network proximity (60%); PPMS shows a more
142 complex profile with presence of centrality (35%), segregation (45%) and cortical proximity (20%); HA
143 matches a combination of centrality (25%), cortical proximity (60%) and constant progression (20%).
144 Credible intervals in the topological profile weights, shown in parentheses in Table 1, reflect the credible
145 intervals explicitly estimated by the GP Progression Model. Variability of the topological profile parameters
146 under bootstrapping with 100 samples are shown in brackets. The reported p-values and effect sizes (in
147 braces) are relative to the null hypothesis of $\beta = 0$ aside from the term associated with the constant
148 progression, computed via permutation testing and Bonferroni-corrected for multiple comparison across the
149 set of network metrics. All p-values were found <0.01 apart from the inverse degree for AD, for which
150 p=0.048. Supplementary Information (Table S1) shows the topological profiles for all 82 brain regions;
151 results remain consistent. Supplementary Information (Table S2) shows the topological profiles for two
152 subsets of the HA cohort, age-matched with the AD and PPMS cohorts, as compared to topological profiles
153 for the whole HA cohort; results remain consistent.

Topological descriptor	Network metrics	AD	PPMS	HA
Centrality	Betweenness centrality	**0.21(0.17)** [0.22(0.18)] {0.01(2.85)}	**0.10(0.08)** [0.11(0.08)] {0.01(2.72)}	0.09(0.06) [0.07(0.05)] {0.01(3.16)}
	Closeness centrality	0.01(0.02) [0.04(0.04)] {0.01(2.90)}	**0.11(0.11)** [0.12(0.12))] {0.01(2.34)}	0.03(0.05) [0.04(0.04)] {0.01(1.79)}
	Weighted degree	0.03(0.03) [0.02(0.02)] {0.01(3.10)}	0.07(0.05) [0.07(0.05)] {0.01(2.96)}	**0.13(0.09)** [0.11(0.07)] {0.01(2.78)}
	Clustering coefficient	**0.19(0.11)**	**0.14(0.05)**	**0.10(0.07)**

		[0.21(0.12)] {0.01(3.32)}	[0.14(0.06)] {0.01(4.52)}	[0.08(0.06)] {0.01(2.97)}
Segregation	Inverse degree	0.05(0.06) [0.05(0.05)] {0.05(0.26)}	**0.17(0.12)** [0.016(0.11)] {0.01(3.43)}	0.01(0.01) [0.01(0.01)] {0.01(5.31)}
	Inverse clustering	0.01(0.03) [0.05(0.04)] {0.01(1.90)}	**<u>0.32(0.22)</u>** [0.36(0.24)] {0.01(2.82)}	0.01(0.01) [0.01(0.02)] {0.01(2.01)}
Network proximity	Shortest path	**<u>0.65(0.39)</u>** [0.54(0.35)] {0.01(3.62)}	0.06(0.06) [0.07(0.06)] {0.01(2.48)}	0.01(0.04) [0.01(0.02)] {0.01(1.48)}
Cortical proximity	Spatial distance	0.06(0.08) [0.10(0.06)] {0.01(2.14)}	**0.22(0.14)** [0.21(0.18)] {0.01(3.22)}	**<u>0.64(0.38)</u>** [0.54(0.32)] {0.01(3.46)}
Constant progression	Constant term	0.07(0.02) [0.12(0.03)] {0.01(4.01)}	0.08(0.04) [0.10(0.05)] {0.01(3.56)}	**0.19(0.09)** [0.18(0.12)] {0.01(3.58)}

Table 1. Weights of the topological profiles of the three cohorts. The table reports the weights for each network metric, grouped per topological descriptor. Credible intervals for the weights are given in parentheses. Bootstrapping variation is shown in square brackets. Bonferroni-corrected p-values and effect size for the permutation testing of the null hypothesis are shown in braces. In bold the weights that have been used to compute the topological profiles.

Topological profiles match disease progression better than any single descriptor

The third row of Figure 2 shows predicted atrophy progression using the best-matching single topological descriptor. Overall, the combinations of descriptors (Figure 2, second row) match the data (Figure 2, first row) more closely than the single best-fitting descriptor (Figure 2, third row). For example, according to the topological profile prediction, the parietal lobe is involved in the early stages of AD, in agreement with the data, while it appears to be involved at a later stage, according to the single best-matching descriptor (network proximity, underlined in Table 1), which also underestimates the involvement of the subcortical areas. Similarly in PPMS, the topological profile prediction reproduces the subcortical involvement better than the best-fitting single descriptor (segregation – inverse clustering). In HA the topological profile prediction shows involvement of the temporal and frontal lobes, as does the atrophy pattern, while the strongest single descriptor (cortical proximity) underestimates subcortical involvement and overestimates parietal involvement. Further, we note that topological profiles explain variance in the data better than the best-fitting single descriptors. Indeed, in the AD cohort, the topological profile explains 82% of the variance, with the constant term explaining just 6%, in contrast to 51% explained by network proximity. In the PPMS cohort, the topological profile explains 83%, the constant term 7%, and inverse clustering 25%. Similarly, in

173 the HA cohort the topological profile explains 88%, the constant term 16%, and cortical proximity 64%. To
174 quantify and compare how well the topological model predictions match the data, we also calculate the
175 Akaike Information Criterion (AIC), which penalizes model complexity [66]. The topological profiles always
176 provide lower AIC scores than the best-fitting single descriptor model (see Supplementary Information,
177 Table S4), thus explaining the data better without overfitting. For full details please refer to the Methods
178 section.

179 Individual profiles group around cohort profiles and separate in topological space

180 Figure 3 plots the cohort-level topological profiles and the individual topological profiles on different
181 topological spaces, for different groups of individuals. Personalized topological profiles come from fitting
182 the best combination of network metrics to individual progression rates. The GP Progression Model provides
183 individual time parameters positioning the individuals along the estimated progression and thus enables the
184 estimation of individual progression rates with respect to the global disease progression (see Methods:
185 Personalized topological profiles).

186 We consider a 5D topological space spanned by each of the five descriptors we consider (centrality,
187 segregation, network proximity, cortical proximity and constant progression). The position of a particular
188 topological profile within this space has coordinates that are the sums of the weights of the network metrics
189 corresponding to each descriptor. The ternary plots in Figures 3(a), 3(c) and 3(e) show the distribution of
190 individual profiles colored according to the cohort to which the individual belongs (red for AD, green for
191 PPMS, blue for HA). The position corresponds to the relative Euclidean distances of the individual profile
192 from each cohort-level profile in the 5D topological space. Thus the corners correspond to exact matches
193 with one of the cohort profiles, while points at the center of the triangle are equidistant to all three cohort-
194 level profiles. Individual profiles that are closer to the profile of another cohort are highlighted as black
195 diamonds with border color reflecting the true cohort; we refer to these individuals as "outliers". Figures
196 3(b), 3(d) and 3(f) show projections of the 5D topological space to 2D using t-Distributed Stochastic
197 Neighbor Embedding (tSNE: [67]), which visualizes high dimensional points in a low dimensional space in a
198 way that retains pairwise similarity with high probability, i.e. most points that are close/distant in the 5D
199 space are close/distant in the 2D visualization. Thus, while the global shapes of the distributions of points
200 have limited interpretation, disconnected groups of points in the tSNE plot reflect separation in the native
201 space. Each tSNE plot shows the cohort-level topological profile from each full cohort (big stars), the
202 variation of the cohort-level topological profile under bootstrap resampling (small stars), and each individual
203 topological profile (dots).

204 Figures 3(a) and 3(b) show the plots for topological profiles computed using the GP Progression
205 Model. They include points for only disease-diagnosed individuals in the disease cohorts (AD or MCI in the
206 AD cohort; PPMS-diagnosed in the PPMS cohort; excluding controls in both), but all individuals from the
207 HA cohort. Figures 3(c) and 3(d) show only the controls from the AD and PPMS cohort, as well as all the
208 HA cohort, also using the topological profiles obtained from the full temporal trajectories. Figures 3(e) and
209 3(f) show the same individuals as Figures 3(a) and 3(b) but using topological profiles derived from only late-
210 stage patient data, mimicking current standard models, which ignore disease progression; see Supplementary
211 Information: Late-stage atrophy modeling. Supplementary Table S3 shows results using random networks to
212 show that the separation is genuinely driven by the underlying structural connectivity.

213 Figures 3(a) and 3(b) show that i) the cohort topological profiles are consistent under bootstrap
214 cross-validation, ii) the three cohorts separate well in topological space, and iii) individual profiles group
215 around cohort profiles.

216 Figures 3(c) and 3(d) and supplementary Table S4 confirm that the separation observed in Figures
217 3(a) and 3(b) is due to disease-related information, and not to differences in MRI centres, MRI scanner or

acquisition protocol, as the three groups of healthy controls show weaker separation than the distinct disease groups.

Matching progression pattern defines profile better than late-stage atrophy alone

Figures 3(e) and 3(f) show that when using only late-stage atrophy to identify topological profiles: i) the cohorts separate less strongly than using the DPM topological profiles (see Table S2); and ii) the rate of assignment of AD and PPMS individual profiles to the corresponding cohort profile is lower than using GP Progression Model-driven topological profiles and with a greater fraction of outliers (see Table 3). Both observations suggest that late-stage information alone is not sufficient to provide distinct topological profiles.

Table 2 shows the weights for the topological profiles when using late-stage data. We observe that, with respect to the topological profiles estimated using the GP Progression Model (Table 1), the centrality components in AD and HA are decreased (from 40% to 25% and from 25% to 15%, respectively), including an increase in uncertainty for all the estimates. In HA we also note an increase in the constant propagation term (from 15% to 30%), which may be explained as a compensatory effect for the decrease of the other weights, as the constant propagation term is analogous to the intercept in linear regression – for details see Methods section.

Table 3 is a confusion matrix of classification rates for subject assignments: without parentheses are the rates for assignment using the GP Progression Model (using patient data only — no controls); numbers in parentheses are the rates when using late-stage information (patients only). These confirm that superior classification rates come from using GP Progression Model driven profiles.

Topological descriptors	Network metrics	AD	PPMS	HA
	Betweenness centrality	0.15(0.11)	0.11(0.09)	0.05(0.02)
Centrality	Closeness centrality	0.01(0.03)	0.06(0.07)	0.01(0.02)
	Weighted degree	0.03(0.04)	0.11(0.08)	0.09(0.05)
	Clustering coefficient	0.07(0.10)	0.11(0.15)	0.03(0.02)
Segregation	Inverse degree	0.06(0.06)	0.12(0.09)	0.06(0.06)
	Inverse clustering	0.09(0.08)	0.25(0.22)	0.01(0.04)
Network proximity	Shortest path	0.30(0.22)	0.05(0.05)	0.02(0.04)
Cortical proximity	Spatial distance	0.12(0.09)	0.15(0.09)	0.15(0.09)
Constant progression	Constant term	0.04(0.05)	0.10(0.07)	0.33(0.21)

Table 2. Weights of the topological profiles of the three cohorts when using only late-stage atrophy data are more uncertain and overlap more. The table reports the weights for each network metric, grouped per topological descriptor.

Assigned cohort

e cohort

	AD	PPMS	HA
AD	84% (57%)	4% (9%)	12% (34%)
PPMS	2% (16%)	68% (45%)	29% (38%)
HA	7% (14%)	2% (12%)	91% (74%)

Table 3. Confusion matrix of classification rates for individuals' assignment to each cohort by matching individual topological profiles to cohort-level topological profiles. Without parentheses: results using full GP Progression Model - driven topological profiles. Within parentheses: results using topological profiles estimated from only late-stage data. Higher numbers are better in diagonal entries (correct assignment), and lower numbers are better in off-diagonal entries (incorrect assignment).

Alzheimer's disease individuals that exhibit individual profiles closer to the healthy aging topological profile perform better in cognitive tests

Figure 3(a) identifies 159 AD-cohort outliers (130 MCI, 29 probable AD) closer to the HA cohort-level profile, out of 1312 MCI+AD patients. We analyzed clinical and demographic information for the AD outliers with respect to the rest of the AD cohort (see Supplementary Table S5a). An ANOVA 1-way test between the two groups was performed and differences were found in MMSE, where the outliers exhibit a higher MMSE score (27.6 ± 1.2 vs 26.1 ± 1.7). Slight differences were found in the Clinical Dementia Rating Scale, with outliers scoring lower (1.8 ± 0.7 vs 2.1 ± 0.3). Both results show that the outliers have reduced cognitive deficits compared to inliers, on average. Further information on the ANOVA results is provided in the Supplementary Table S5a. The same analysis performed on the outliers defined by late-stage-driven topological profiles did not report any significant differences between the groups, suggesting that outliers defined using the GP Progression Model-driven topological profiles depart more genuinely from the disease cohort and phenotype of typical amnestic AD; see the Supplementary Table S6a).

Healthy ageing individuals that exhibit individual profiles closer to the AD topological profile show signs of prodromal dementia

Figure 3(a) identifies 358 of 5463 HA individuals closer to the AD cohort profile. An ANOVA 1-way test between these outliers and the rest of the HA group found differences in MMSE, where the outliers exhibit a lower MMSE score (27.7 ± 0.8 vs 28.0 ± 0.6); and a difference in age, with the outliers being older (70.5 ± 10.1 vs 64.5 ± 9.8). No significant difference in gender or APOE status (see Supplementary Table S5c) was found. In order to investigate whether the increased cognitive deficit in the HA outliers indicates an actual prodromal phase of dementia, or is just an age-related effect, we analyzed the incidence, in the outlier group, of the individuals that were healthy at baseline, but developed dementia after 2-4 years (see Methods: Participants - HA). Of those 148 individuals, 105 reside in the HA-AD outlier group, which thus contains 70% of the individuals with prodromal dementia; in contrast the non-outlier group consists of only 5% prodromal dementia cases. The same analysis performed on the outliers defined by late-stage-driven topological profiles reports only a group difference in age with older outliers (65.2 ± 10.9 vs 60.0 ± 7.0). No other significant differences were found (see Supplementary Table S6c)).

Primary progressive multiple sclerosis outliers show no significant differences with the rest of the group

We also analyzed PPMS with respect to both AD and HA: the analysis returned 53 AD individuals closer to PPMS; 1 PPMS individual closer to AD; 13 PPMS individuals closer to HA and 100 HA individuals closer

277 to PPMS. No significant differences were found between any subgroups, for any comparisons: we analyzed
278 age, gender, expanded disability status scale (EDSS) and disease duration when looking at PPMS outliers in
279 AD or HA; age, gender, APOE4 and MMSE score when looking at HA outliers in PPMS; age, gender, years
280 of education, MMSE, ADAS-Cog, APOE4, CDRSB, AV45, when looking at AD outliers in PPMS. Details
281 can be found in Supplementary Table S5b). The same analysis on late-stage-driven topological profiles also
282 returned no significant differences (Supplementary Table S6b).

283 Features derived from the topological profile correlate with clinical features

284 Finally and more generally, we analyzed features extracted from topological profiles, in particular, the
285 distance of individual profiles from the cohort profile, and show that they correlate negatively with
286 individual cohort-specific clinical features. Specifically, MMSE for the AD cohort (R=0.11, p<0.01); EDSS
287 for PPMS (R=0.68, p=0.07); and age for HA (R=0.32, p<0.01).

Discussion

289 We have introduced a novel method to estimate cohort and individual-level topological profiles of
290 neurodegeneration using computational disease progression models in combination with imaging data sets.
291 The profiles give new insight into the relationship between brain connectivity and the progression pattern of
292 neurodegeneration. We demonstrate the ideas using three cohorts representing different neurological
293 conditions: AD, PPMS, HA. We showed that combinations of topological descriptors explain observations
294 better than any individual descriptor and that the combinations representative of each condition, despite
295 some commonality as suggested in [6–8], differ substantially both at the cohort and individual level. We
296 emphasize that these differences go beyond simple observations that the pattern of atrophy accumulation is
297 different in these three cohorts, which could arise simply from equivalent spreading mechanisms from
298 different epicentres; our results go further by strongly suggesting distinct modes of dependence of the
299 pathological spread on the underlying connectivity. We also show that using the full disease time-course,
300 estimated via a GP Progression Model [59] produces better-defined topological profiles than using only late-
301 stage atrophy. This highlights a key weakness in previous state-of-the-art results using late-stage atrophy
302 alone, which can be ameliorated using recent advances in disease progression modeling. Further, we
303 retrieved significant correlation between features of the topological profiles and individual clinical or
304 demographic features, suggesting potential clinical utility of the topological profile. Finally, we showed that
305 the outliers in the AD-HA comparison display characteristics that align them with the other cohort, providing
306 evidence that our topological profiles reflect underlying disease processes, and indicating potential use of the
307 topological profile to highlight disease risk.

308   As discussed in the introduction, one key implication here (as in previous literature[3,20,68,69]) is that
309 graph-theoretic measures may associate with different mechanisms of disease spread in neural networks.
310 Specifically, centrality represents nodal stress (vulnerability of brain hubs), segregation trophic failure
311 (vulnerability of isolated regions), network proximity transneuronal spread of a prion-like agent along
312 network connections, and cortical proximity unguided diffusive propagation [5]. While we draw on these
313 potential links in the following sections, it is important to note that the links between the mathematical
314 abstraction and the biological mechanisms are simplistic, and graph-theory metrics do not fully capture or
315 explain the range of potential spreading mechanisms.

316 The centrality component in AD topological profiles becomes apparent when taking into account the
317 temporal evolution of atrophy

318 The AD topological profile identified here supports recent results that identify neuronal distance from
319 epicentre (or trans-neuronal spread) as the principal topological descriptor of neurodegeneration in AD
320 [7,14,17,20,23]. However, both cohort- and individual-level profiles also show a substantial additional component

of neurodegeneration due to centrality metrics — vulnerability of brain network hubs. This component has not clearly been highlighted previously, because a) it is less apparent in a topological profile estimated from only late-stage atrophy data, and b) it is suppressed when using the previous single-descriptor approach. We found contrasting importance of centrality metrics between full-disease-course and end-stage-only profiles. This might arise from metabolic demand increasing primarily during early degeneration so that hub-vulnerability drives early phases of the progression pattern [70], while neuronal distance from the epicentre dominates later stages. This finding might also explain some aspects of the biological heterogeneity of AD, which produces high variance in atrophy patterns across individuals. In particular, the early centrality component of the topological profile suggests that pathology may start around local hubs, which is consistent with the focal presentation of atrophy in atypical Alzheimer's diseases such as posterior cortical atrophy or progressive aphasia [71–73]. Once established, each disease then spreads through the same broad networks, leading to syndromic convergence in advanced stages of AD.

Similarly, in HA and PPMS, hub vulnerability appears as a significant component only when considering the full trajectory rather than only late-stage atrophy. This may suggest that activity-dependent mechanisms, such as oxidative stress [74], microglial activation [75,76], neurovascular dysfunction [37] or "virtual hypoxia" [38] influence early brain loss across a range of neurodegenerative conditions.

More generally, the differences we observe between full-disease-course and end-stage-only profiles emphasize the importance of considering the full temporal trajectory in assessing the likelihood of potential propagation mechanisms.

Degree of alignment of individual profiles with cohort profiles informs on patient status

Our results indicate that departures of individual profiles from that of the corresponding cohort may signal abnormality with respect to their cohort, while alignment with another cohort-level profile may correspond to clinical features of that other cohort. For example, the AD individuals with a topological profile close to the HA cohort-level profile show on average lower cognitive deficit than the full AD cohort. On the other hand, HA individuals with topological profiles that tend towards the AD cohort-level profile exhibit reduced MMSE score, suggesting cognitive impairment; also, a substantial proportion (70%) of the HA prodromal-dementia individuals (who developed dementia in 2-4 year follow-up) lie in the outlier group, suggesting evidence of neurodegenerative mechanisms consistent with AD. We emphasize again that we identify these outliers using the topological descriptors that explain the atrophy pattern, and not on the atrophy pattern itself, with the intention of highlighting individuals showing abnormal mechanisms of pathology propagation with respect to their cohort.

We found no significant difference in clinical features between PPMS outliers, tending towards either AD or HA, compared with the rest of the PPMS group: topological profiles seem to identify differences among PPMS subjects that are invisible to the available demographic and clinical features (age, gender, EDSS and diseases duration). However, sample sizes are low (N=1 PPMS-AD outlier; N=13 PPMS-HA outliers). Further investigation on a larger cohort of progressive MS subjects, as well as with a broader class of clinical features, may clarify whether the variation we observe in topological profiles arise from spurious effects, or are genuinely informative on the clinical status of the outliers beyond what the available clinical features can identify. For example, future studies of older and longer-term PPMS patients could test the hypothesis that individual topological profiles may inform on co-morbidities, e.g. for an MS-patient who shows signs of dementia, their profile position with respect to the AD cohort profile may inform on whether the dementia comes from MS-related neurodegeneration or AD comorbidity. However, we cannot test this hypothesis here, as our PPMS cohort are "early" PPMS (they were recruited to this study within 5 years of diagnosis), and no subject reported dementia as would be expected[77] although a detailed cognitive assessment was not performed, this agrees.

Neurodegeneration in AD and PPMS is not simply an acceleration of the aging process

Overall, our results suggest that neurodegeneration in AD and PPMS is not simply an acceleration of the aging process, but that the two diseases have distinct topological profiles of neurodegeneration, which differ from those of HA. The cohort and individual-level topological profiles we identify for AD and PPMS are clearly distinct from one another. The AD topological profile is a combination of centrality and network proximity, while the PPMS profile has diverse contributing mechanisms including centrality, segregation and cortical proximity, suggesting that many different processes are at play. Also, both separate from the HA topological profile, which has a strong component of both the cortical proximity and the constant propagation mechanisms, suggesting relatively uniform loss across the brain that is not linked to any particular brain-connectivity feature.

Further, we note that we have regressed out the effects of ageing in the AD and PPMS cohort in order to minimize the effects of the ageing process on disease models. Nevertheless, some components of ageing might still appear in the model for both, which is one key reason for including the HA model for comparison.

These observations underline the idea that mechanisms, in addition to actual atrophy patterns, are distinct in these diseases from those underpinning normal aging.

Future Work

Here we provide a proof of concept of the idea of topological profiling through image-analysis and temporal disease progression modeling, and a demonstration of its potential utility. Multiple opportunities arise for future refinements of the methods, as well as extensions and applications of the key ideas.

Methodologically, several steps in the processing pipeline can limit the accuracy of the network metrics in representing neurodegenerative mechanisms. For example, structural connectome estimation using tractography is prone to false positive and negative connections [78,79] that can influence subsequent predictions. Nevertheless, tractography does reliably recover at least many of the major known anatomical connections sufficiently well to highlight broad differences in atrophy patterns associated to the different mechanisms. Anatomically-constrained probabilistic tractography coupled with SIFT-ing should provide more accurate predictions than deterministic tractography [78,80–83], but future work might consider better ways to mitigate errors e.g. by quantifying uncertainty in tractography output.

Here we take an average connectome over multiple young and healthy individuals as the substrate for pathology propagation. By doing so, we do not account for any influence of the pathology on the connectome itself [51], as some other models attempt to [2,18,51,84,85]. However, we believe this to be a reasonable anatomical reference of a "pure" underlying substrate of propagation to investigate grey matter loss and decide to avoid deliberately the additional complexity of white matter disruptions, which are not well understood and would complicate the model substantially. This decision is also supported by recent results in AD showing that the choice of connectome (young and healthy or subject-specific) does not significantly impact the predictive ability of a model for trans-synaptic transmission of toxic proteins [86]. However, future models could approximate reductions of connectivity arising from white matter damage commensurate with grey-matter atrophy, but this requires a clear picture of the interaction of such processes, e.g. from disease progression models of regional grey-matter atrophy and white-matter integrity. We believe using the healthy connectome as the substrate for propagation is a sensible first-order approximation.

One major advantage of our approach for evaluating topological descriptors is that it considers group-level longitudinal information on atrophy rather than considering only late-stage atrophy patterns. Our method uses each network metric to obtain a scalar value at each graph node that provides a template of the rate of pathology accrual at that node compared to others, and then compares to rate-of-change of atrophy

410 evolution as estimated by the GP Progression Model. Future work may extend the idea by accounting for
411 variable change over time, which will need to compare the full temporal evolution of atrophy to the full
412 temporal evolution induced by each topological descriptor. One additional caveat of using the GP
413 Progression Model is that the model captures the trajectory of change in biomarker values rather than
414 underlying pathology; differences among biomarker accuracy (e.g. higher noise in volume measurements of
415 smaller regions) can make the order of biomarker change depart from the order of underlying pathological
416 change, although we expect such effects tend to be small with our processing pipeline – see [44,55] for further
417 discussion.

418   Our approach does not account for heterogeneity within cohorts. In addition to variation in the
419 structural connectome discussed above, the epicentre for disease propagation may vary among patients in a
420 particular disease class and a number of recent works explore methods for per-subject epicentre selection
421 [54,87]. Here we estimated a single cohort-level epicentre as the most atrophied region for each data set, and
422 each reflected common knowledge of brain tissue loss in AD, PPMS and HA. Our epicentres broadly agree
423 with [5], who found that individually-selected epicentres in a number of neurodegenerative diseases are always
424 seated in or near the most atrophied region. Recent data-driven approaches [88] further reveal within-cohort
425 heterogeneity of temporal trajectories, which our current approach does not accommodate, but such advances
426 provide great potential for future work to focus topological profiling on more homogeneous subgroups and
427 to explore the variability of topological profiles among different disease subgroups. Indeed, we believe
428 application to broader cohorts, as for instance generic progressive MS including both primary and secondary
429 (which would be more numerous) would require better identification of distinct subgroups than the
430 traditional MS classifications (clinically isolated syndrome, relapsing remitting MS, and primary and
431 secondary progressive MS), and methods such as SuStain[88] would offer a way to identify within-cohort
432 subtypes for better topological profile estimation. As concerns applications to prodromal phases of diseases –
433 an example being radiologically isolated syndrome for MS – future work will be devoted to build models of
434 the whole neurodegeneration process within specific diseases and their subtypes defined by distinct
435 trajectories of pathological change, which might be used for instance for discriminating subjects that convert
436 to degeneration from others that do not, thereby informing treatment and care choices.

437   The ideas we propose here extend to a much larger range of diseases and disease subtypes and offer
438 a new and unique tool to exploit the full power of large imaging data sets in exposing mechanisms of disease
439 aetiology and propagation. With further development and experiments, topological profiles may also provide
440 useful information in the clinic. For example, AD-like HA outliers may be considered at risk for AD and
441 decisions could be informed by this, including patient management (more frequent visits to monitor the
442 patient) and recruitment into clinical studies/trials.

443   The underlying models of propagation remain simplistic and a great many alternative descriptors and
444 mechanisms could easily be included, such as propagation via functional networks [5,17], or different kinds of
445 tractography to represent intra and extra-axonal propagation [25,26,51]. Simplicity of the models and limitations
446 of processing steps is important to bear in mind while interpreting results, and validation, e.g. against
447 histological analysis in animal models [89], is an important future target to establish the extent to which
448 mechanistic information inferred in this way matches low-level observations of molecular propagation.

Materials and Methods

450 Our pipeline for creating topological profiles in a neurodegenerative condition is the following.
451 1) Generate an average structural connectome from young healthy data.
452 2) Pre-process the cohort data to adjust for nuisance variables and generate the longitudinal data for regional
453 atrophy and topology, relative to healthy controls.
454 3) Build the DPM and topological profile.

455 We now describe the data and these steps in detail.

Data Description

Participants – AD

458 The data used in the preparation of this article were obtained from the Alzheimer's disease Neuroimaging
459 Initiative (ADNI) database (adni.loni.usc.edu). The ADNI was launched in 2003 as a public-private
460 partnership, led by Principal Investigator Michael W. Weiner, MD. The primary goal of ADNI has been to
461 test whether serial Magnetic Resonance Imaging (MRI), Positron Emission Tomography (PET), other
462 biological markers, and clinical and neuropsychological assessment can be combined to measure the
463 progression of MCI and early AD. For up-to-date information, see www.adni-info.org. We collected
464 longitudinal measurements for all the available ADNI 1/GO/2 individuals with at least one "quality control"
465 flagged 3D-T1 MRI scan. Repeated T1-weighted structural MRI images were acquired at 3T machines
466 across multiple centers according to a harmonized protocol. Longitudinal FreeSurfer was used to align
467 images from multiple time-points according to subject specific median templates, in order to avoid temporal
468 bias. Subject with no available diagnosis were discarded, thus leaving us 1713 subjects, with "HC", "MCI"
469 or "AD" diagnosis. We collected longitudinal FreeSurfer 5.1 volume data on all the GM and subcortical
470 regions from ADNIMERGE.csv. For information on scanning protocols and segmentation algorithms see
471 www.adni-info.org. The subjects included in our analysis are 1713; the mean (std) age of the cohort is
472 73.9(7.2) years. The overall scans are 6670; the average (std) time between scans is 2.4(1.8) years. More
473 information are in the Supplementary Information (Figure 3-figure supplement 1 and Table S7).

Participants – PPMS

475 This was a retrospective study of 64 participants, studied at the UCL Queen Square Institute of Neurology in
476 London. The participants include 44 individuals with primary progressive multiple sclerosis (PPMS) and 20
477 healthy controls (HC). We collected longitudinal FreeSurfer 5.1 volumetric data on all the GM and
478 subcortical regions. For information on scanning protocol, segmentation algorithms, please refer to [90]. The
479 longitudinal data set used for this study consisted in 64 individuals; the mean (std) age of the cohort is
480 41.6(10.2) years. The overall scans are 244 scans; the average (std) time between scans is 4.0(1.5) years.
481 More information are in the Supplementary Information (Figure 3-figure supplement 1 and Table S8).

Participants – HA

483 The data used in the preparation of this article were obtained from The Rotterdam Scan Study [91,92]. The
484 Rotterdam Study is a prospective cohort study ongoing since 1990 in the city of Rotterdam in The
485 Netherlands. The study targets cardiovascular, endocrine, hepatic, neurological, ophthalmic, psychiatric,
486 dermatological, otolaryngology, locomotor, and respiratory diseases. Initially, in 1995 and 1999, random
487 subsamples of participants from the Rotterdam Study underwent neuroimaging, whereas from 2005 onwards
488 brain MRI has been implemented into the core protocol of the Rotterdam Study. We excluded individuals
489 with prevalent dementia at study entry, and individuals presenting cortical infarcts on the MRI. The study
490 contains 148 individuals that would develop dementia in the 2-4 years follow-up(s). We leave them in the
491 study as we are interested to model their individual topological profiles with respect to the topological profile
492 of the cohort-level. We collected longitudinal FreeSurfer 5.1 volumetric data on all the GM and subcortical
493 regions. For information on the scanning protocols and segmentation algorithms see [92]. The longitudinal data
494 set used for this study consisted in 5463 individuals; the mean (std) age of the cohort is 64.8(10.8) years. The
495 overall scans are 11627 scans; the average (std) time between scans is 5.3(1.1) years. More information are
496 in the Supplementary Information (Figure 3-figure supplement 1 and Table S9).

Data pre-processing to obtain model inputs

498 On each data set of volumetric GM and subcortical regions separately, we performed three steps:

499 1) Adjustment for nuisance variables: we constructed a regression model for each region separately with
500 volumes as dependent variable and total intracranial volume, gender, and age (age not included for the HA
501 cohort) as independent variables.

502 2) Variable selection: from the original FreeSurfer Regions of Interest (ROIs) we discarded white matter,
503 brain stem, ventricular and cerebellar regions, leaving 82 ROIs. Then, we averaged the (adjusted) volumes of
504 each region from both hemispheres, obtaining 41 bilateral regions.

505 3) Z–scores computation: we computed z–scores against a control population. For the AD data set, the
506 control population was formed by the "HC"-diagnosed individuals; for the HA cohort it was formed by the
507 "Young" individuals (those whose age is more than one standard deviation less than the mean age); for the
508 PPMS data set it was formed by the "HC"-diagnosed individuals.

509 HCP participants

510 Data used in the preparation of this work were obtained from the MGH-USC Human Connectome Project
511 (HCP) database (ida.loni.usc.edu/login.jsp). The HCP project (Principal Investigators: Bruce Rosen, M.D.,
512 Ph.D., Martinos Center at Massachusetts General Hospital; Arthur W. Toga, Ph.D., University of California,
513 Los Angeles, Van J. Weeden, MD, Martinos Center at Massachusetts General Hospital) is supported by the
514 National Institute of Dental and Cranio-facial Research (NIDCR), the National Institute of Mental Health
515 (NIMH) and the National Institute of Neurological Disorders and Stroke (NINDS). Collectively, the HCP is
516 the result of efforts of co-investigators from the University of California, Los Angeles, Martinos Center for
517 Biomedical Imaging at Massachusetts General Hospital (MGH), Washington University, and the University
518 of Minnesota. The data set consisted of 24 unique subjects: we collected raw high–resolution 3D T1–
519 weighted and DTI of 24 age and gender–matched subjects (age: 26, 50% female).

520 Connectome generation

521 Structural connectomes were generated using tools provided in the MRtrix3 software package
522 (http://mrtrix.org). The pipeline included [51]: DWI denoising [93], pre-processing [94] and bias–field correction
523 [95]; inter–modal registration [96]; T1 tissue segmentation [60]; spherical deconvolution [97,98]; probabilistic
524 tractography [99] utilizing anatomically-constrained tractography [100], dynamic seeding and SIFT [98]; T1
525 parcellation [60]; robust structural connectome construction [101]. Our anatomical connectome for each
526 participant is a weighted adjacency matrix that includes only inter-node connections across the 82 ROIs
527 consisting of cortical and subcortical gray-matter regions, excluding the cerebellum and brain stem. The
528 average structural adjacency matrix was computed by taking the mean over the subject-wise matrices.
529 Weights, or connection strengths, were normalized to [0, 1]. The inter-hemisphere average is performed after
530 the network metrics computation step (see below).

531 Mathematical modeling

532 Network metrics

533 We selected five different descriptors of graph topology (centrality, segregation, network proximity cortical
534 proximity and constant progression) and 9 metrics across these categories[102]:

535   1. Centrality measures:

536   a) Weighted degree: the sum of the weights of the connections incident the node of
537   interest.

538   b) Betweenness centrality: the number of shortest paths between any two nodes that
539   pass through the specific node.

540   c) Closeness centrality: the inverse of the path length between the node of interest and
541   all the other nodes.

542   d) Clustering coefficient: the proportion of triangular sub-networks formed by the node
543   and its neighboring nodes.

544   2. Segregation measures:

545   a) Inverse of weighted degree.

546   b) Inverse of clustering coefficient.

547   3. Network proximity:

548   a) Shortest path to epicenter.

549   4. Cortical proximity:

550   a) Spatial distance from epicenter.

551   5. Constant progression:
552   a) Constant term quantifying to what extent the rate of atrophy remains constant
553   throughout the progression.

554 Each network metric produces a scalar value for each node that indicates its vulnerability to pathology
555 relative to all other nodes. Each thus leads to a temporal progression pattern in which the accumulation of
556 pathology, e.g. the atrophy or rate of change of volume, is proportional to that vulnerability (see Figure 4). In
557 order to identify the epicenters needed to compute 3a) and 4a), we selected, for each subject, the region with
558 the highest z-scores of GM volumes (i.e. the "most atrophied" region) in the last follow-up MRI scan; the
559 cohort-level epicenters are then, for each cohort, the regions that most frequently appear as individual-level
560 epicenters. They are the hippocampus (AD), the caudate (PPMS) and the insula (HA). These epicenters are
561 supported by literature in AD [5,103], PPMS [42,62] and HA [104–108].

562   We computed the first 7 network metrics using the Brain Connectivity Toolbox [109] in MATLAB,
563 after appropriate normalization (*weight_conversion* function). To compute the cortical proximity metric,
564 which does depend on the structural connections, we select the segmented structural MRIs in the HCP
565 cohort, and measure the (average) pairwise cortical distances between all the macro-regions' barycenters
566 (using the *mris_pmake* command in FreeSurfer). The constant progression metric, which also does not
567 depend on the structural connections, simply assigns a constant value to each region.

568   We note that the network metrics computing similar attributes of a graph such as centrality and
569 efficiency, or segregation and inefficiency, are not independent and in fact highly correlated producing
570 strongly overlapping progression patterns. However, we include multiple network metrics for certain
571 topological descriptors to capture variability in the corresponding progression pattern that fits within the
572 definition of the descriptor.

573   Network metrics were computed on the average structural adjacency matrix formed of 82 ROIs, and
574 then averaged across hemisphere, obtaining an array of 9 metrics for each of the 41 symmetrized
575 regions v, $\boldsymbol{g}(v) = \left(g_1(v), \ldots, g_9(v)\right)^T$, where we set $g_9(v) = 1$ to describe the constant progression term.

GP progression model

Continuous Disease Progression Models (DPM) aim to estimate the long-term temporal pattern of disease progression directly from short-term longitudinal data sets and to stage patients based on individual observations. The problem is challenging, due to the lack of a well-defined temporal reference in longitudinal data sets: time of onset is usually unknown and rate of pathology accrual is highly variable in most neurodegenerative conditions. DPM techniques typically tackle this problem by assuming that each visit at which measurements are taken occurs at an unknown "disease time", the particular value of which for each individual subject is a hidden variable estimated while fitting the set of trajectories. The disease-time axis parametrizes the natural evolution of the pathology common to all individuals.

The models usually assume mixed effects, in which the long-term trajectories are the fixed effect (represented by parametric or non-parametric functions), and the individual variations from the group-level trajectories are the random effects. Further, individual time reparametrization parameters (also known as time warp parameters[53] or disease scores[41,46]) are estimated by quantifying the individual positions with respect to the estimated time-frame. Here, we use the GP Progression Model of [59], which is a non-parametric Bayesian mixed effect model, to estimate long-term trajectories of regional GM volumes on each data set (AD, PPMS and HA) separately. Figure 5 shows a pictorial example of the GP Progression Model combined with the topological profiles procedure.

Formally, if we represent by $(X^j(t_1), \dots, X^j(t_K^j))^T$ the longitudinal measurements of the regional GM volumes associated with each individual j at their $(t_1, \dots, t_K^j)$ absolute time points (i.e. dates of subject visit or subject's age-at-visit), and consider all measurements obtained at a particular visit of one individual to occur at a particular disease time τ_k^j, where the mapping from absolute time t to disease time τ is via a subject-specific time reparametrization function, which here is just a simple shift: $t_k^j = \tau_k^j + d^j$, then the observations for subject j at a single time point t (indices omitted but implied) can be modelled as a random sample from the GP Progression Model:

$$X^j(t) := \left(X_1^j(t), \dots, X_V^j(t) \right)^T$$
$$= f(t) + n^j(t) + E. \#(1)$$

Here $f(t) = (f_1(t), \dots, f_V(t))^T$ is the fixed effect function modeling the longitudinal evolution of the V GM volumes, and is modeled as a Gaussian Process; $n^j(t) = \left(n^j_1(t), \dots, n^j_V(t) \right)^T$ are the individual random effects; and $E = (E_1, \dots, E_V)^T$ is the observational noise. The model is described in detail in [59] together with the optimization scheme to recover the probabilistic estimates of the parameters for the fixed effect, the random effect, and the individual time reparametrization parameters. Identifiability of the model is ensured by enforcing monotonicity on the population-level biomarker trajectories f_v.

Fitting the model also provides an estimate of the highest rate of change of each biomarker during the disease progression. That is the maximum of the derivatives of the estimated trajectories f_v along the disease time τ:

$$Y_v = \max_\tau f_v'(\tau), \#(2)$$

for each biomarker $v \in \{1, \dots, V\}$. Existence and boundness of Y_v is guaranteed by the finiteness of the time-shifts, which is enforced by the smoothness of the Gaussian Process. Indeed, for each subject j, d^j defines the optimal shift of the data point on the temporal time axis. The estimates of these positions must be compatible with the Gaussian Process describing the temporal trajectory (Figure 2-figure supplement 2, 3 and 4). Gaussian processes are completely identified by the kernel function (in our case a radial basis function - RBF), which prescribes the shape and smoothness of the interpolating curve via its length-scale l

615 and variance σ. For this reason, the relative positions (i.e. the time-shifts) of each individual are naturally
616 bounded by the length-scale of the Gaussian process, so the only compatible solutions are those with the
617 time-shifts softly constrained to a finite range determined by $2l$. The monotonicity constraint on f_v
618 guarantees uniqueness of Y_v for each v. The model returns uncertainty on $\boldsymbol{f}$, which can be projected to $\boldsymbol{f'}$ and
619 thus $\boldsymbol{Y}$.

Topological profile estimate

621 We estimate the topological profile $\boldsymbol{\beta}$ by identifying the unique combination of topological descriptors that
622 best matches the GP Progression. This means estimating the weights $\boldsymbol{\beta}$ from the linear model

$$Y = \Sigma\boldsymbol{\beta} + \boldsymbol{\varepsilon}, \#(3)$$

623 where $\boldsymbol{Y} = (Y_1, \ldots, Y_V)^T$; $\boldsymbol{\Sigma}$ collects the values of the metrics $\boldsymbol{g}(v)$ for every region v, i.e.
624 $\boldsymbol{\Sigma} = (\boldsymbol{g}(1), \ldots, \boldsymbol{g}(V))^T$; and $\boldsymbol{\varepsilon}$ is the noise. As a first step we normalize both $\boldsymbol{Y}$ and $\boldsymbol{\Sigma}$ to the range [0, 1]. We
625 also enforce non-negativity of $\boldsymbol{\beta}$, so that β_n can be precisely interpreted as the weight with which descriptor
626 n contributes to the overall observed pattern of neurodegeneration $\boldsymbol{Y}$. Our problem is then the one of
627 estimating $\boldsymbol{\beta}$ such that:

$$\boldsymbol{\beta} = argmax_{\boldsymbol{\beta} \geq 0} L(\boldsymbol{Y}, \boldsymbol{\Sigma}\boldsymbol{\beta}), \#(4)$$

628 where L is the likelihood of the model, which assumes Gaussian noise, so that (4) becomes equivalent to
629 constrained least-squares minimization. We solve the problem via Expectation-Maximization, which, in the
630 positively-constrained least-squared case, has a simple closed form, and becomes an iterative-multiplicative
631 algorithm also known as ISRA[110,111].

Personalized topological profiles

633 For each subject, the GP Progression Model estimates a set of time-points τ_k^j describing the subject's
634 measurements in the new disease time $\boldsymbol{\tau}$ as $t_k^j = \tau_k^j + d^j$, where d^j is the subject-specific shift. If we define
635 the subject temporal position in the disease time as the shifted average age $\widetilde{\tau^j}$, where $\widetilde{t^j} = \widetilde{\tau^j} + d^j$ and $\widetilde{t^j}$ is
636 the average age of subject j across age-at-visits, then we can compute the individual speed of progression
637 along the disease time as

$$Y_v^j = f_v'(\widetilde{\tau^j}), \qquad \#(5)$$

638 for each biomarker $v \in \{1, \ldots, V\}$. These values encode information on the individual rates of change along
639 the disease progression. We can then estimate the individual topological profile $\boldsymbol{\beta^j}$ by identifying the unique
640 combination of topological descriptors that best matches the individual progression as

$$\boldsymbol{\beta^j} = argmax_{\boldsymbol{\beta^j} \geq 0} L(\boldsymbol{Y^j}, \boldsymbol{\Sigma}\boldsymbol{\beta^j}), \#(6)$$

641 where $\boldsymbol{Y^j} = (Y_1^j, \ldots, Y_V^j)^T$. As in the cohort-level framework, the problem can be solved, for each subject j,
642 via ISRA.

Model selection

644 In order to quantify the performances of the topological profiles progression against the single-best fitting
645 descriptor in reproducing the observed progression from the GP Progression Model, we compute Aikake
646 Information Criterion (AIC) for each model to balance error scores with model complexity. We assume
647 Gaussian noise and set $AIC = 2N + V\log(\frac{RSS}{V})$, where N is the number of model parameters, V is the number
648 of data points (GM regions), and the RSS is the residual sum of squares between the predicted outcome of

17

the model and the data, i.e. $\sum_{v=1}^{V}((\boldsymbol{Y} - \boldsymbol{\Sigma\beta})^2)_v$. The single-best fitting descriptor choice has just one parameter, with trans-neuronal spread or proximity spread having one additional parameter for epicenter selection. The topological profiles have one parameter for each descriptor, plus one parameter for epicenter selection, minus one parameter as the weights are normalized, i.e. as many parameters as the number of the descriptors. The AIC scores are in Supplementary Information Table S4.

Data availability

AD data set from ADNI. ADNI is a public-private partnership. All ADNI data are shared without embargo through the LONI Image and Data Archive (https://ida.loni.usc.edu/login.jsp) a secure research data repository. Interested scientists may obtain access to ADNI imaging, clinical, genomic, and biomarker data for the purposes of scientific investigation, teaching, or planning clinical research studies. Access is contingent on adherence to the ADNI Data Use Agreement. For up-to-date information please see http://adni.loni.usc.edu/wp-content/uploads/how_to_apply/ADNI_DSP_Policy.pdf.

PPMS data set from UCLH. Data can be obtained upon request, directed the management team of the data at the Institute of Neurology, UCL: uclh.qsmsc@nhs.net.

HA data set from the Rotterdam Study. Data can be obtained upon request. Requests should be directed towards the management team of the Rotterdam Study (secretariat.epi@erasmusmc.nl), which has a protocol for approving data requests. Because of restrictions based on privacy regulations and informed consent of the participants, data cannot be made freely available in a public repository. The Rotterdam Study has been approved by the Medical Ethics Committee of the Erasmus MC (registration number MEC 02.1015) and by the Dutch Ministry of Health, Welfare and Sport (Population Screening Act WBO, license number 1071272-159521-PG). The Rotterdam Study has been entered into the Netherlands National Trial Register (NTR; www.trialregister.nl) and into the WHO International Clinical Trials Registry Platform (ICTRP; www.who.int/ictrp/network/primary/en/) under shared catalogue number NTR6831. All participants provided written informed consent to participate in the study and to have their information obtained from treating physicians.

HCP data are from the Human Connectome Project. Open Access Data (all imaging data and most of the behavioral data) is available to those who register an account at ConnectomeDB and agree to the Open Access Data Use Terms. This includes agreement to comply with institutional rules and regulations. For up-to-date information please see https://www.humanconnectome.org/study/hcp-young-adult/data-use-terms.

AD, PPMS and HA processed, anonymized and unrecognizable data, useful to process the mechanistic weights can be obtained upon request to the corresponding author: sara.garbarino@inria.fr.

Code availability

Code is available at: https://github.com/sgarbarino/mechanistic-profiles.

The software (BrainPainter) for coloring brain images as in Figure 2 is open-source and available at: https://github.com/mrazvan22/brain-coloring.

Acknowledgments

Declaration of competing interests

721 The authors declare no competing interests.

References

723 1.   Iturria-Medina, Y. Anatomical Brain Networks on the Prediction of Abnormal Brain States. *Brain*
724   *Connect.* **3**, 1–21 (2013).

725 2.   Iturria-Medina, Y. & Evans, A. C. On the central role of brain connectivity in neurodegenerative
726   disease progression. *Front. Aging Neurosci.* **7**, 1–10 (2015).

727 3. Raj, A., Kuceyeski, A. & Weiner, M. A Network Diffusion Model of Disease Progression in
728   Dementia. *Neuron* **73**, 1204–1215 (2012).

729 4. Seeley, W. W., Crawford, R. K., Zhou, J., Miller, B. L. & Michael, D. Neurodegenerative diseases
730   target large-scale human brain networks. *Neuron* **62**, 42–52 (2009).

731 5. Zhou, J., Gennatas, E. D., Kramer, J. H., Miller, B. L. & Seeley, W. W. Predicting Regional
732   Neurodegeneration from the Healthy Brain Functional Connectome. *Neuron* **73**, 1216–1227 (2012).

733 6. Soto, C. & Pritzkow, S. Protein misfolding, aggregation, and conformational strains in
734   neurodegenerative diseases. *Nat. Neurosci.* **21**, 1332–1340 (2018).

735 7. Jucker, M. & Walker, L. C. Propagation and spread of pathogenic protein assemblies in
736   neurodegenerative diseases. *Nat. Neurosci.* **21**, 1341–1349 (2018).

737 8. Fu, H., Hardy, J. & Duff, K. E. Selective vulnerability in neurodegenerative diseases. *Nat. Neurosci.*
738   **21**, 1350–1358 (2018).

739 9. Buckner, R. L. *et al.* Cortical hubs revealed by intrinsic functional connectivity: mapping, assessment
740   of stability, and relation to Alzheimer's disease. *J. Neurosci.* **29**, 1860–73 (2009).

741 10. Saxena, S. & Caroni, P. Selective Neuronal Vulnerability in Neurodegenerative Diseases: from
742   Stressor Thresholds to Degeneration. *Neuron* **71**, 35–48 (2011).

743 11. Appel, S. H. A unifying hypothesis for the cause of amyotrophic lateral sclerosis, parkinsonism, and
744   alzheimer disease. *Ann. Neurol.* **10**, 499–505 (1981).

745 12. Salehi, A. *et al.* Increased App Expression in a Mouse Model of Down's Syndrome Disrupts NGF
746   Transport and Causes Cholinergic Neuron Degeneration. *Neuron* **51**, 29–42 (2006).

747 13. Frost, B. & Diamond, M. I. Prion-like mechanisms in neurodegenerative diseases. *Nature Reviews*
748   *Neuroscience* **11**, 155–159 (2010).

749 14. Jucker, M. & Walker, L. C. Self-propagation of pathogenic protein aggregates in neurodegenerative
750   diseases. *Nature* **501**, 45–51 (2013).

751 15. Prusiner, S. B. Some Speculations about Prions, Amyloid, and Alzheimer's Disease. *N. Engl. J. Med.*
752   **310**, 661–663 (1984).

753 16. Buckner, R. L. *et al.* Molecular, structural, and functional characterization of Alzheimer's disease:
754   evidence for a relationship between default activity, amyloid, and memory. *J. Neurosci.* **25**, 7709–17
755   (2005).

756 17. Cope, T. E. *et al.* Tau burden and the functional connectome in Alzheimer's disease and progressive
757   supranuclear palsy. *Brain* **141**, 550–567 (2018).

758 18. Fornito, A., Zalesky, A. & Breakspear, M. The connectomics of brain disorders. *Nat. Rev. Neurosci.*
759   **16**, 159–172 (2015).

760 19. Mancini, M. *et al.* Network attack simulations in Alzheimer's disease: The link between network
761   tolerance and neurodegeneration. in *2016 IEEE 13th International Symposium on Biomedical*
762   *Imaging (ISBI)* 237–240 (IEEE, 2016). doi:10.1109/ISBI.2016.7493253

763 20. Raj, A. *et al.* Network Diffusion Model of Progression Predicts Longitudinal Patterns of Atrophy and
764   Metabolism in Alzheimer's Disease. *Cell Rep.* **10**, 359–369 (2015).

765 21. Raj, A. *et al.* A Network Diffusion Model of Disease Progression in Dementia. *Neuron* **73**, 1204–
766   1215 (2013).

767 22. Iaccarino, L. *et al.* Local and distant relationships between amyloid, tau and neurodegeneration in
768   Alzheimer's Disease. *NeuroImage Clin.* **17**, 452–464 (2018).

769 23. Weickenmeier, J., Jucker, M., Goriely, A. & Kuhl, E. A physics-based model explains the prion-like
770   features of neurodegeneration in Alzheimer's disease, Parkinson's disease, and amyotrophic lateral
771   sclerosis. *J. Mech. Phys. Solids* **124**, 264–281 (2019).

772 24. Mišić, B. *et al.* Cooperative and Competitive Spreading Dynamics on the Human Connectome.
773   *Neuron* **86**, 1518–1529 (2015).

774 25. Iturria-Medina, Y., Carbonell, F. M., Sotero, R. C., Chouinard-Decorte, F. & Evans, A. C.
775   Multifactorial causal model of brain (dis)organization and therapeutic intervention: Application to
776   Alzheimer's disease. *Neuroimage* **152**, 60–77 (2017).

777 26. Iturria-Medina, Y., Carbonell, F. M. & Evans, A. C. Multimodal imaging-based therapeutic
778   fingerprints for optimizing personalized interventions: Application to neurodegeneration. *Neuroimage*
779   **179**, 40–50 (2018).

780 27. Jones, D. T. *et al.* Cascading network failure across the Alzheimer's disease spectrum. *Brain* **139**,
781   547–562 (2016).

782 28. Leal, S. L., Lockhart, S. N., Maass, A., Bell, R. K. & Jagust, W. J. Subthreshold Amyloid Predicts
783   Tau Deposition in Aging. *J. Neurosci.* **38**, 4482–4489 (2018).

784 29. Steenwijk, M. D. *et al.* Cortical atrophy patterns in multiple sclerosis are non-random and clinically
785   relevant. *Brain* **139**, 115–126 (2016).

786 30. Irwin, D. J., Lee, V. M. Y. & Trojanowski, J. Q. Parkinson's disease dementia: Convergence of α-
787   synuclein, tau and amyloid-β pathologies. *Nature Reviews Neuroscience* **14**, 626–636 (2013).

788 31. Lei, P. *et al.* Tau protein: Relevance to Parkinson's disease. *International Journal of Biochemistry
789   and Cell Biology* **42**, 1775–1778 (2010).

790 32. Arai, T. *et al.* Phosphorylated TDP-43 in Alzheimer's disease and dementia with Lewy bodies. *Acta
791   Neuropathol.* **117**, 125–136 (2009).

792 33. Hamilton, R. L. Lewy Bodies in Alzheimer's Disease: A Neuropathological Review of 145 Cases
793   Using α-Synuclein Immunohistochemistry. *Brain Pathol.* **10**, 378–384 (2006).

794 34. Spires-Jones, T. L., Attems, J. & Thal, D. R. Interactions of pathological proteins in
795   neurodegenerative diseases. *Acta Neuropathol.* **134**, 187–205 (2017).

796 35. Attems, J. & Jellinger, K. A. The overlap between vascular disease and Alzheimer's disease - lessons
797   from pathology. *BMC Med.* **12**, 206 (2014).

798 36. Kalaria, R. N. Neurodegenerative disease: Diabetes, microvascular pathology and Alzheimer disease.
799   *Nat. Rev. Neurol.* **5**, 305–6 (2009).

800 37. Sweeney, M. D., Kisler, K., Montagne, A., Toga, A. W. & Zlokovic, B. V. The role of brain
801   vasculature in neurodegenerative disorders. *Nat. Neurosci.* **21**, 1318–1331 (2018).

802 38. Trapp, B. D. & Stys, P. K. Virtual hypoxia and chronic necrosis of demyelinated axons in multiple
803   sclerosis. *Lancet Neurol.* **8**, 280–291 (2009).

804 39. Oxtoby, N. P. & Alexander, D. C. Imaging plus X. *Curr. Opin. Neurol.* **30**, 371–379 (2017).

805 40. Bilgel, M., Prince, J. L., Wong, D. F., Resnick, S. M. & Jedynak, B. M. A multivariate nonlinear
806   mixed effects model for longitudinal image analysis: Application to amyloid imaging. *Neuroimage*

807   **134**, 658–670 (2016).

808 41. Donohue, M. C. *et al.* Estimating long-term multivariate progression from short-term data.
809   *Alzheimer's Dement.* **10**, S400–S410 (2014).

810 42. Eshaghi, A. *et al.* Progression of regional grey matter atrophy in multiple sclerosis. *Brain* **141**, 1665–
811   1677 (2018).

812 43. Firth, N. C. *et al.* Data-driven disease progression modelling using neurophysiological tests Posterior
813   Cortical Atrophy vs Alzheimer's disease. *Alzheimer's Dement.* **12**, P963–P964 (2016).

814 44. Fonteijn, H. M. *et al.* An event-based model for disease progression and its application in familial
815   Alzheimer's disease and Huntington's disease. *Neuroimage* **60**, 1880–1889 (2012).

816 45. Iturria-Medina, Y. *et al.* Early role of vascular dysregulation on late-onset Alzheimer's disease based
817   on multifactorial data-driven analysis. *Nat. Commun.* **7**, (2016).

818 46. Jedynak, B. M. *et al.* A computational neurodegenerative disease progression score: Method and
819   results with the Alzheimer's disease neuroimaging initiative cohort. *Neuroimage* **63**, 1478–1486
820   (2012).

821 47. Koval, I. *et al.* Statistical learning of spatiotemporal patterns from longitudinal manifold-valued
822   networks. in *Lecture Notes in Computer Science (including subseries Lecture Notes in Artificial*
823   *Intelligence and Lecture Notes in Bioinformatics)* **10433 LNCS**, 451–459 (Springer, Cham, 2017).

824 48. Li, D., Iddi, S., Thompson, W. K. & Donohue, M. C. Bayesian latent time joint mixed effect models
825   for multicohort longitudinal data. *Statistical Methods in Medical Research* 096228021773756 (2017).
826   doi:10.1177/0962280217737566

827 50. Marinescu, R. V. *et al.* DIVE: A spatiotemporal progression model of brain pathology in
828   neurodegenerative disorders. *Neuroimage* **192**, 166–177 (2019).

829 51. Oxtoby, N. P. *et al.* Data-driven sequence of changes to anatomical brain connectivity in sporadic
830   Alzheimer's disease. *Front. Neurol.* **8**, (2017).

831 52. Oxtoby, N. P. *et al.* Data-driven models of dominantly-inherited Alzheimer's disease progression.
832   *Brain* **141**, 1529–1544 (2018).

833 53. Schiratti, J.-B., Allassonnière, S., Colliot, O. & Durrleman, S. A Bayesian Mixed-Effects Model to
834   Learn Trajectories of Changes from Repeated Manifold-Valued Observations. *J. Mach. Learn. Res.*
835   **18**, 1–33 (2017).

836 54. Venkatraghavan, V., Bron, E., Niessen, W. & Klein, S. A Discriminative Event Based Model for
837   Alzheimer's Disease Progression Modeling. 121–133 (2017).

838 55. Young, A. L. *et al.* A data-driven model of biomarker changes in sporadic Alzheimer's disease. *Brain*
839   **137**, 2564–2577 (2014).

840 56. Hinrichs, C., Singh, V., Xu, G. & Johnson, S. C. Predictive markers for AD in a multi-modality
841   framework: An analysis of MCI progression in the ADNI population. *Neuroimage* **55**, 574–589
842   (2011).

843 57. Moradi, E., Pepe, A., Gaser, C., Huttunen, H. & Tohka, J. Machine learning framework for early
844   MRI-based Alzheimer's conversion prediction in MCI subjects. *Neuroimage* **104**, 398–412 (2015).

845 58. Nie, L. *et al.* Modeling Disease Progression via Multisource Multitask Learners: A Case Study With
846   Alzheimer's Disease. *IEEE Trans. Neural Networks Learn. Syst.* **28**, 1508–1519 (2017).

847   59.   Lorenzi, M. *et al.* Probabilistic disease progression modeling to characterize diagnostic uncertainty:
848   Application to staging and prediction in Alzheimer's disease. *Neuroimage* **190**, 56–68 (2019).

849   60.   Desikan, R. S. *et al.* An automated labeling system for subdividing the human cerebral cortex on MRI
850   scans into gyral based regions of interest. *Neuroimage* **31**, 968–980 (2006).

851   61.   Braak, H. & Braak, E. Staging of Alzheimer's disease-related neurofibrillary changes. *Neurobiol.*
852   *Aging* **16**, 271–8; discussion 278-84 (1995).

853   62.   Eshaghi, A. *et al.* Deep gray matter volume loss drives disability worsening in multiple sclerosis.
854   *Ann. Neurol.* **83**, 210–222 (2018).

855   63.   Vinke, E. J. *et al.* Trajectories of imaging markers in brain aging: the Rotterdam Study. *Neurobiol.*
856   *Aging* **71**, 32–40 (2018).

857   64.   Narvacan, K., Treit, S., Camicioli, R., Martin, W. & Beaulieu, C. Evolution of deep gray matter
858   volume across the human lifespan. *Hum. Brain Mapp.* **38**, 3771–3790 (2017).

859   65.   Watson, R., Colloby, S. J., Blamire, A. M. & O'Brien, J. T. Subcortical volume changes in dementia
860   with Lewy bodies and Alzheimer's disease. A comparison with healthy aging. *Int. Psychogeriatrics*
861   **28**, 529–536 (2016).

862   66.   Akaike, H. A new look at the statistical model identification. *IEEE Trans. Automat. Contr.* **19**, 716–
863   723 (1974).

864   67.   Maaten, L. van der & Hinton, G. Visualizing Data using t-SNE. *J. Mach. Learn. Res.* **9**, 2579–2605
865   (2008).

866   68.   Zhou, J., Gennatas, E. D., Kramer, J. H., Miller, B. L. & Seeley, W. W. Predicting Regional
867   Neurodegeneration from the Healthy Brain Functional Connectome. *Neuron* **73**, 1216–1227 (2012).

868   69.   Seeley, W. W., Crawford, R. K., Zhou, J., Miller, B. L. & Greicius, M. D. Neurodegenerative
869   Diseases Target Large-Scale Human Brain Networks. *Neuron* **62**, 42–52 (2009).

870   70.   de Haan, W., Mott, K., van Straaten, E. C. W., Scheltens, P. & Stam, C. J. Activity Dependent
871   Degeneration Explains Hub Vulnerability in Alzheimer's Disease. *PLoS Comput. Biol.* **8**, e1002582
872   (2012).

873   71.   Alladi, S. *et al.* Focal cortical presentations of Alzheimer's disease. *Brain* **130**, 2636–2645 (2007).

874   72.   Du, A.-T. *et al.* Different regional patterns of cortical thinning in Alzheimer's disease and
875   frontotemporal dementia. *Brain* **130**, 1159–1166 (2006).

876   73.   Mendez, M. F., Ghajarania, M. & Perryman, K. M. Posterior cortical atrophy: clinical characteristics
877   and differences compared to Alzheimer's disease. *Dement. Geriatr. Cogn. Disord.* **14**, 33–40 (2002).

878   74.   Barnham, K. J., Masters, C. L. & Bush, A. I. Neurodegenerative diseases and oxidative stress. *Nat.*
879   *Rev. Drug Discov.* **3**, 205–214 (2004).

880   75.   Cagnin, A. *et al.* In-vivo measurement of activated microglia in dementia. *Lancet* **358**, 461–467
881   (2001).

882   76.   Hickman, S., Izzy, S., Sen, P., Morsett, L. & El Khoury, J. Microglia in neurodegeneration. *Nat.*
883   *Neurosci.* **21**, 1359–1369 (2018).

884   77.   Chiaravalloti, N. D. & DeLuca, J. Cognitive impairment in multiple sclerosis. *Lancet Neurol.* **7**,
885   1139–1151 (2008).

886 78. Maier-Hein, K. H. *et al.* The challenge of mapping the human connectome based on diffusion
887   tractography. *Nat. Commun.* **8**, 1349 (2017).

888 79. Thomas, C. *et al.* Anatomical accuracy of brain connections derived from diffusion MRI tractography
889   is inherently limited. *Proc. Natl. Acad. Sci. U. S. A.* **111**, 16574–9 (2014).

890 80. Petersen, M. V. *et al.* Probabilistic versus deterministic tractography for delineation of the cortico-
891   subthalamic hyperdirect pathway in patients with Parkinson disease selected for deep brain
892   stimulation. *J. Neurosurg.* **126**, 1657–1668 (2017).

893 81. Descoteaux, M., Deriche, R., Knosche, T. R. & Anwander, A. Deterministic and Probabilistic
894   Tractography Based on Complex Fibre Orientation Distributions. *IEEE Trans. Med. Imaging* **28**,
895   269–286 (2009).

896 82. Tsai, S.-Y. Reproducibility of structural brain connectivity and network metrics using probabilistic
897   diffusion tractography. *Sci. Rep.* **8**, 11562 (2018).

898 83. Daducci, A., Dal Palú, A., Descoteaux, M. & Thiran, J.-P. Microstructure Informed Tractography:
899   Pitfalls and Open Challenges. *Front. Neurosci.* **10**, 247 (2016).

900 84. Fornari, S., Schafer, A., Jucker, M., Goriely, A. & Kuhl, E. Prion-like spreading of Alzheimer's
901   disease within the brain's connectome. *bioRxiv* 529438 (2019). doi:10.1101/529438

902 85. Zeighami, Y. *et al.* Network structure of brain atrophy in de novo parkinson's disease. *Elife* **4**, 1–20
903   (2015).

904 86. Powell, F. *et al.* Preserved Structural Network Organization Mediates Pathology Spread in
905   Alzheimer's Disease Spectrum Despite Loss of White Matter Tract Integrity. *J. Alzheimer's Dis.* **65**,
906   747–764 (2018).

907 87. Acosta, D., Powell, F., Zhao, Y. & Raj, A. Regional vulnerability in Alzheimer's disease: The role of
908   cell-autonomous and transneuronal processes. *Alzheimers. Dement.* **14**, 797–810 (2018).

909 88. Young, A. L. *et al.* Uncovering the heterogeneity and temporal complexity of neurodegenerative
910   diseases with Subtype and Stage Inference. *Nat. Commun.* **9**, 4273 (2018).

911 89. Mezias, C. & Raj, A. Analysis of Amyloid-β Pathology Spread in Mouse Models Suggests Spread Is
912   Driven by Spatial Proximity, Not Connectivity. *Front. Neurol.* **8**, 653 (2017).

913 90. Eshaghi, A. *et al.* Temporal and spatial evolution of grey matter atrophy in primary progressive
914   multiple sclerosis. *Neuroimage* **86**, 257–264 (2014).

915 91. Hofman, A. *et al.* The Rotterdam Study: 2016 objectives and design update. *Eur. J. Epidemiol.* **30**,
916   661–708 (2015).

917 92. Ikram, M. A. *et al.* The Rotterdam Scan Study: design update 2016 and main findings. *Eur. J.
918   Epidemiol.* **30**, 1299–1315 (2015).

919 93. Veraart, J., Fieremans, E. & Novikov, D. S. Diffusion MRI noise mapping using random matrix
920   theory. *Magn. Reson. Med.* **00**, n/a-n/a (2015).

921 94. Andersson, J. L. R. & Sotiropoulos, S. N. An integrated approach to correction for off-resonance
922   effects and subject movement in diffusion MR imaging. *Neuroimage* **125**, 1063–1078 (2016).

923 95. Tustison, N. J. *et al.* N4ITK: Improved N3 bias correction. *IEEE Trans. Med. Imaging* **29**, 1310–1320
924   (2010).

925 96. Modat, M. *et al.* Global image registration using a symmetric block-matching approach. *J. Med.*

926   *Imaging* **1**, 024003 (2014).

927   97.   Jeurissen, B., Tournier, J. D., Dhollander, T., Connelly, A. & Sijbers, J. Multi-tissue constrained
928   spherical deconvolution for improved analysis of multi-shell diffusion MRI data. *Neuroimage* **103**,
929   411–426 (2014).

930   98.   Smith, R. E., Tournier, J. D., Calamante, F. & Connelly, A. SIFT: Spherical-deconvolution informed
931   filtering of tractograms. *Neuroimage* **67**, 298–312 (2013).

932   99.   Tournier, J.-D. & , F. Calamante, and a. C. Improved probabilistic streamlines tractography by 2 nd
933   order integration over fibre orientation distributions. *Ismrm* **88**, 2010 (2010).

934   100.   Smith, R. E., Tournier, J. D., Calamante, F. & Connelly, A. Anatomically-constrained tractography:
935   Improved diffusion MRI streamlines tractography through effective use of anatomical information.
936   *Neuroimage* **62**, 1924–1938 (2012).

937   101.   Yeh, C. H., Smith, R. E., Liang, X., Calamante, F. & Connelly, A. Correction for diffusion MRI fibre
938   tracking biases: The consequences for structural connectomic metrics. *Neuroimage* **142**, 150–162
939   (2016).

940   102.   Bullmore, E. & Sporns, O. Complex brain networks: Graph theoretical analysis of structural and
941   functional systems. *Nat. Rev. Neurosci.* **10**, 186–198 (2009).

942   103.   Lehmann, M. *et al.* Intrinsic connectivity networks in healthy subjects explain clinical variability in
943   Alzheimer's disease. *Proc. Natl. Acad. Sci.* **110**, 11606–11611 (2013).

944   104.   Abe, O. *et al.* Aging in the CNS: Comparison of gray/white matter volume and diffusion tensor data.
945   *Neurobiol. Aging* **29**, 102–116 (2008).

946   105.   Allen, J. S., Damasio, H. & Grabowski, T. J. Normal neuroanatomical variation in the human brain:
947   An MRI-volumetric study. *Am. J. Phys. Anthropol.* **118**, 341–358 (2002).

948   106.   Good, C. D. *et al.* A voxel-based morphometric study of ageing in 465 normal adult human brains.
949   *Neuroimage* **14**, 21–36 (2001).

950   107.   Kalpouzos, G. *et al.* Voxel-based mapping of brain gray matter volume and glucose metabolism
951   profiles in normal aging. *Neurobiol. Aging* **30**, 112–124 (2009).

952   108.   Tisserand, D. J. *et al.* A voxel-based morphometric study to determine individual differences in gray
953   matter density associated with age and cognitive change over time. *Cereb. Cortex* **14**, 966–73 (2004).

954   109.   Rubinov, M. & Sporns, O. Complex network measures of brain connectivity: Uses and
955   interpretations. *Neuroimage* **52**, 1059–1069 (2010).

956   110.   Daube-Witherspoon, M. E. & Muehllehner, G. An Iterative Image Space Reconstruction Algorthm
957   Suitable for Volume ECT. *IEEE Trans. Med. Imaging* **5**, 61–66 (1986).

958   111.   Dempster, A., Laird, N. & Rubin, D. Maximum likelihood from incomplete data via the EM
959   algorithm. *J. R. Stat. Soc. Ser. B Stat. Methodol.* 1–38 (1977).

960 # Figure legends

961 Figure 1. Overview of topological profile estimation. (a) we construct the average structural connectome
962 from Human Connectome Project (HCP) tractograms; (b) we compute topological descriptors on the
963 structural connectome and the progression pattern that corresponds to each; (c) we estimate the long-term
964 atrophy progression pattern and its variability within each condition, using GP Disease Progression Model
965 on regional volumes from T1-weighted MRI ; (d) we estimate rates of progression for each individual from

the cohort-level GP progression model; (e) we estimate each topological profile (both cohort-level and individual) as the linear combination of topological descriptors, with weights $\boldsymbol{\beta}$, that best matches the observed progression rates. Those profiles are then visualized in a low-dimensional projection of the space of topological descriptors.

Figure 2. Temporal evolution of brain loss in AD, PPMS and HA confirm known atrophy progression patterns, and the progression patterns corresponding to the topological profiles for the three cohorts match the progression of atrophy better than the single best fitting topological descriptor. Top row: 4D representation of the GP disease progression model for AD (left), PPMS (middle) and HA (right). Second row: 4D representation of the progression pattern corresponding to the topological profile for AD (left) - a combination of centrality measures and network-based proximity; PPMS (middle) – a combination of centrality, segregation and cortical proximity measures; and HA (right) - a combination of centrality, cortical proximity, and constant progression. Third row: 4D representation of the progression pattern corresponding the single best fitting topological descriptor for AD (left) - network proximity; PPMS (middle) - segregation; and HA (right) - cortical proximity. Each region's color opacity is proportional to the cumulative abnormality of each region (strong blue means strongly atrophied), and time increases from left to right. AIC is the Aikake Information Criterion for the fit to the observed disease progression (lower is better).

Figure 3. Individual profiles are specific for each neurological condition. Red indicates AD individuals, blue indicates HA and green is PPMS. Panel (a) shows ternary plot of the individual profiles, obtained via the GP Progression Model, for AD+MCI-diagnosed individuals, PPMS-diagnosed individuals, and HA individuals plotted according to the distance from the cohort-level profile; corners are cohort-level profiles. Outliers of each cohort are highlighted (identified with diamonds); (b) shows a 2D representation of the topological profiles in (a), using tSNE; big stars represent the cohort profiles and small ones the bootstrapped cohort-profiles; (c) ternary plot using GP Progression Model -driven profiles for only healthy control individuals in the AD and PPMS cohorts, and HA individuals; (d) tSNE plot of data in (c); (e) ternary plot of the individual profiles for AD+MCI-diagnosed, PPMS-diagnosed, and HA individuals, estimated from only late-stage data; (f) tSNE plot for the topological profiles of data in (e).

Figure 4: Temporal progression patterns (left-to-right) of different descriptors. For each descriptor (row), abnormality increases in a descriptor-specific pattern. The magnitude of cumulative abnormality at a node is proportional to the color intensity. Red nodes are epicenters. (a) Centrality: node A is affected first due to having the highest centrality, followed by node B, then C and D. (b) Segregation: node D is affected first due to having the highest segregation, followed by C, then B and A. (c) Network proximity: nodes B and C are affected before D, because they are closer to the epicenter A (along the connectivity network). (d) Cortical proximity: node B is affected first because of its spatial proximity to the epicenter A, then C and finally D. Here edges are dashed as no information is needed from connectivity.

Figure 5: A schematic representation of the mathematical modeling of the topological profiling with GP Progression Model. In the example here we have three biomarkers/regions (represented in red ($v = 1$), green ($v = 2$) and blue ($v = 3$)), and two topological descriptors (g and h). a) The GP Progression Model estimates temporal trajectories of biomarkers progression, along the disease time $\boldsymbol{\tau}$. The unique maximum points of the derivatives of the trajectories correspond to their maximal rate of change $\boldsymbol{Y}$. b) Two topological descriptors are computed for each region from anatomical connectomes. They combine, column-wise, in the matrix $\boldsymbol{\Sigma}$. c) For each subject j, the GP Progression Model estimates a time-reparametrization which shifts individual measurements to the disease time. For each biomarker, the speed of progression of subject j with respect to the cohort progression is the value of the derivative of the biomarker progression at $\widetilde{\tau}^j$, which represents the shift of the average age of the subject. d) Topological profiles are estimated via a linear model relating $\boldsymbol{\Sigma}$ and $\boldsymbol{Y}$ (for the cohort-level topological profile) or $\boldsymbol{Y}^j$ (for the individual profiles).

Supplementary Figure legends

Figure 2–figure supplement 1. Fine-grained representation of Figure 2, with 12 stages. Top row, for each panel: 4D representation of the disease progression model for AD (top panel), PPMS (middle panel) and HA (bottom panel). Middle row, for each panel: 4D representation of the progression corresponding to the topological profiles for AD (top panel), combination centrality and network proximity; PPMS (middle panel), combination of segregation, centrality and cortical proximity; and HA (bottom panel), combination of centrality and cortical proximity spread. Bottom row, for each panel: 4D representation of the progression corresponding to the single best fitting descriptors for AD (top panel), network proximity to epicenter; PPMS (middle panel), segregation - inverse clustering specifically; HA (bottom panel), cortical proximity. Each region's color is proportional to the cumulative abnormality of each region, and time reads from left to right. In red rectangles, the regions selected for Fig 2, main text.

Figure 2–figure supplement 2. Biomarker trajectories, with standard deviations and measurements for the AD cohort. Here in full red the estimated trajectories and in dashed red the standard deviations (1-sigma confidence band). Each colored dot is a individual, and is colored according to the baseline diagnosis (magenta = HC, green = MCI, black = AD). The model estimates a time-shift ("Re-parameterized age") that shuffles the individuals disaggregating the diagnosis (i.e. HC individual are earlier in the progression, followed by MCI, and then AD).

Figure 2–figure supplement 3. Individual trajectories, with standard deviations and measurements, for the PPMS cohort. Estimated trajectories in full red and in dashed red the standard deviations (1-sigma confidence band). Each colored dot is a individual, and is colored according to the baseline diagnosis (magenta = HC, green = PPMS). The model estimates a time-shift ("Re-parameterized age") that shuffles the individuals disaggregating the diagnosis (i.e. HC individual are earlier in the progression, followed by PPMS).

Figure 2–figure supplement 4. Individual trajectories, with standard deviations and measurements, for the HA cohort. Estimated trajectories in full red and in dashed red the standard deviations (1-sigma confidence band). Each colored dot is a individual, and is colored according to the baseline age: magenta < mean-std (Young" cohort); mean-std<green<mean+std; black > mean+std ("Old" cohort).

Figure 3-figure supplement 1. Longitudinal information for the study cohort (AD: 1713 individuals, HA 5463 individuals, PPMS 64 individuals). The overall time-points are 6670 for AD, 11627 for HA and 244 for PPMS; the average follow-up (years) are 2.4 for AD, 5.3 for HA and 4.0 for PPMS; the standard deviation of follow-up (years) is 1.8 for AD, 1.1 for HA and 1.5 for PPMS; the range of follow-up (years) is 0.5-10 for AD, 0.7-10.5 for HA and 0-6 for PPMS.

Supplementary File 1. Supplementary file comprising Tables S1-S9.

Figure 1

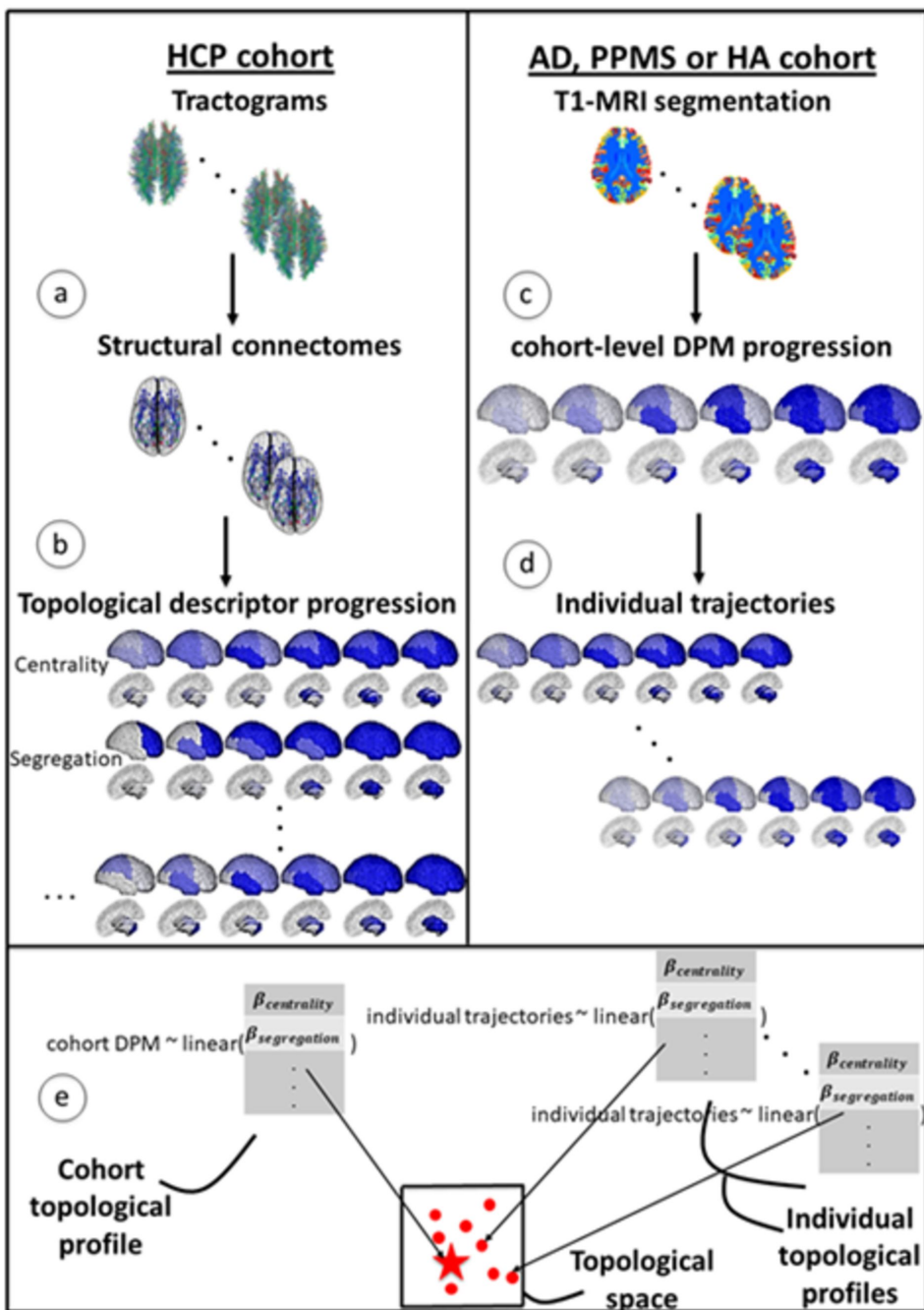**HCP cohort**

Tractograms

(a)

Structural connectomes

(b)

Topological descriptor progression

Centrality

Segregation

...

AD, PPMS or HA cohort

T1-MRI segmentation

(c)

cohort-level DPM progression

(d)

Individual trajectories

...

(e)

cohort DPM ~ linear($\beta_{centrality}$, $\beta_{segregation}$, ...)

individual trajectories ~ linear($\beta_{centrality}$, $\beta_{segregation}$, ...)

individual trajectories ~ linear($\beta_{centrality}$, $\beta_{segregation}$, ...)

Cohort topological profile

Topological space

Individual topological profiles
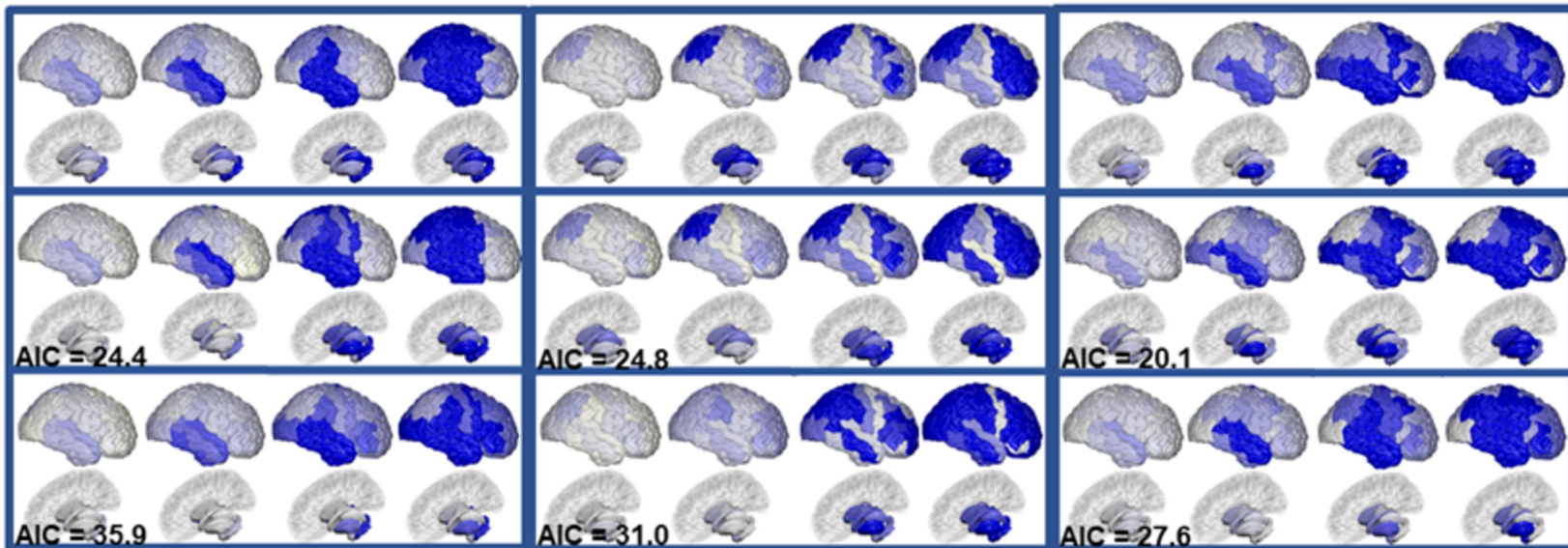
Figure 2

Figure 3

GP progression model-driven profiles (patients)
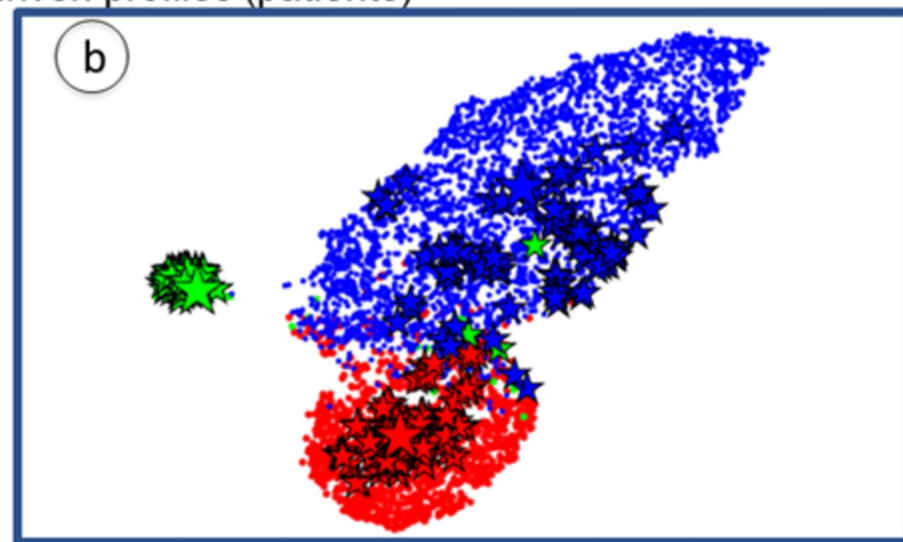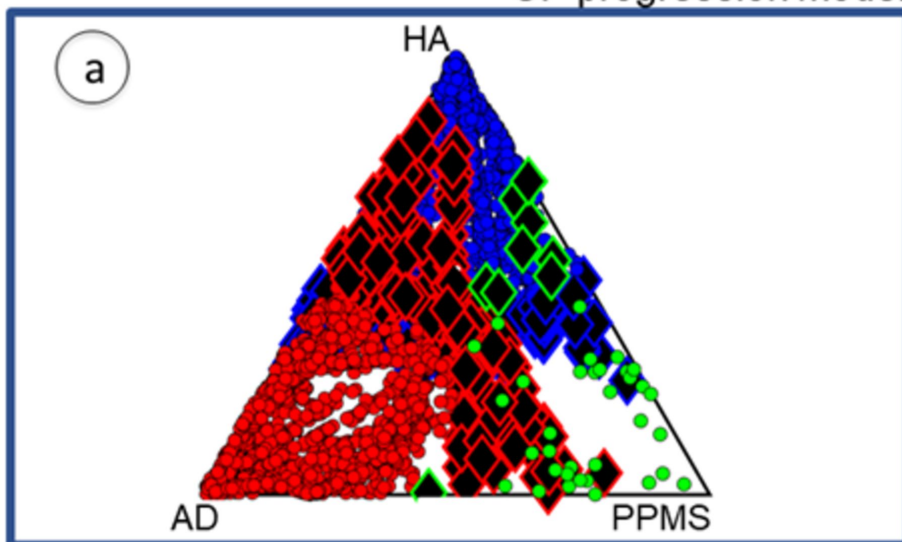
GP progression model-driven profiles (controls)
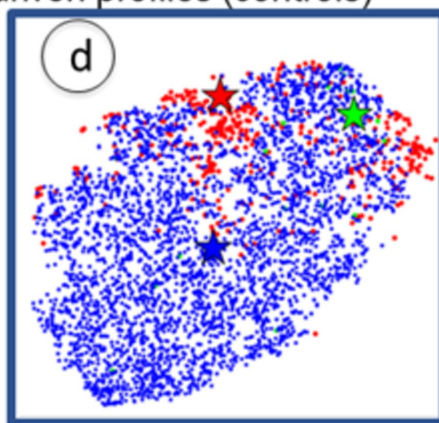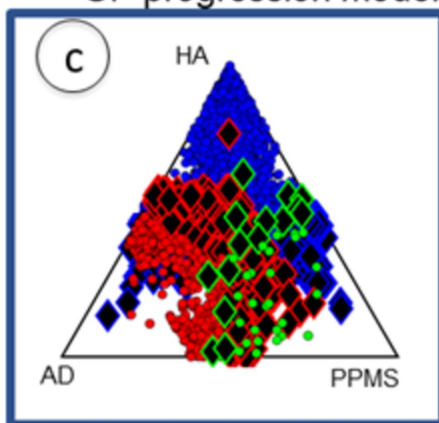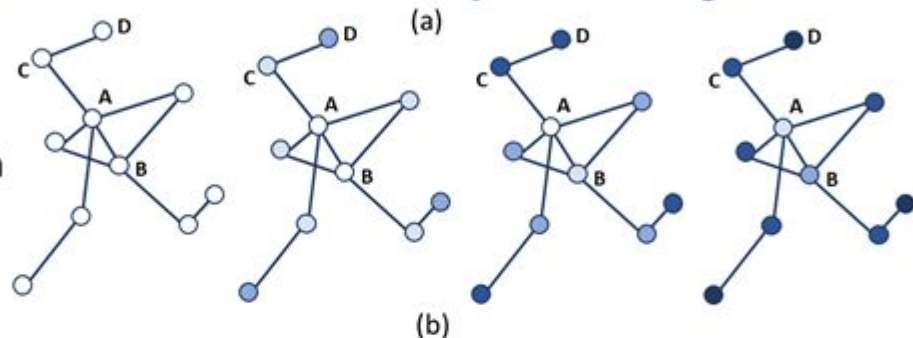
Late-stage-driven profiles (patients)
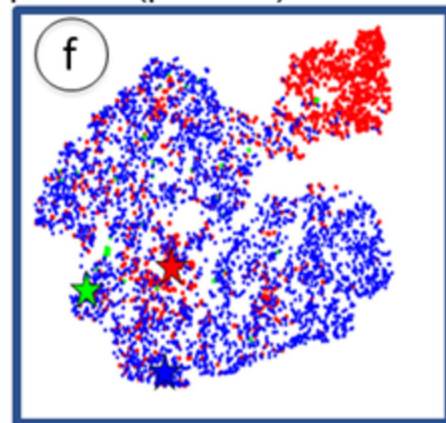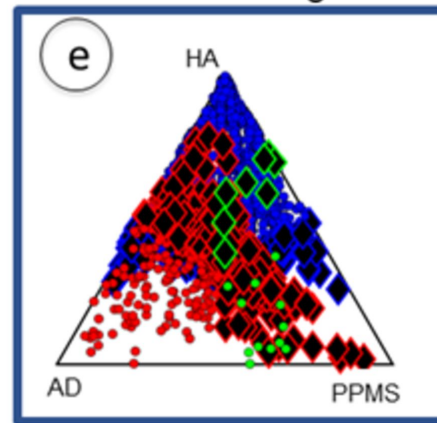
Figure 4

Centrality (a)
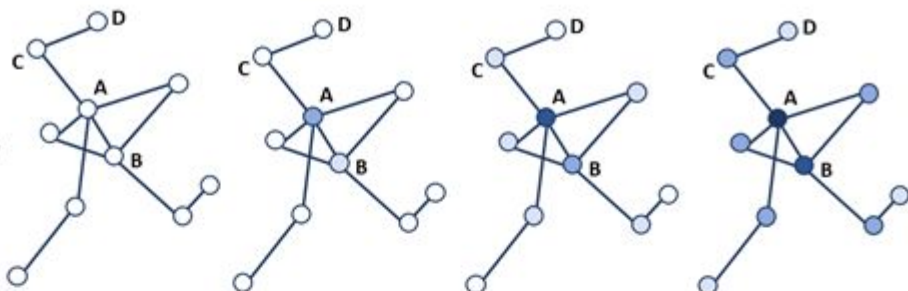
Segregation (b)

Network proximity (c)

Cortical proximity (d)

Abnormality

Figure 5

GP Progression Model – cohort-level progression

Biomarkers' measurements

Rate of change

Y_1
Y_2
Y_3

τ

$\boldsymbol{Y} = (Y_1, Y_2, Y_3)^{\boldsymbol{T}}$

$\boldsymbol{Y} = \boldsymbol{\Sigma}\boldsymbol{\beta}$

$\boldsymbol{\beta} = (\beta_g, \beta_h)^{\boldsymbol{T}}$

Cohort-level topological profiles

Topological descriptor progression

descriptor g

g_1
g_3
g_2

descriptor h

h_1
h_3
h_2

$\boldsymbol{\Sigma} = \begin{bmatrix} g_1 & h_1 \\ g_2 & h_2 \\ g_3 & h_3 \end{bmatrix}$

Individualization procedure

Biomarkers' measurements

Rate of change

Y_2^j
Y_1^j
Y_3^j

$\widetilde{\tau}^j$

$\boldsymbol{Y}^j = (Y_2^j, Y_1^j, Y_3^j)^{\boldsymbol{T}}$

$\boldsymbol{Y}^j = \boldsymbol{\Sigma}\boldsymbol{\beta}^j$

$\boldsymbol{\beta}^j = (\beta_g^j, \beta_h^j)^{\boldsymbol{T}}$

Individual topological profiles

a

b

c

d
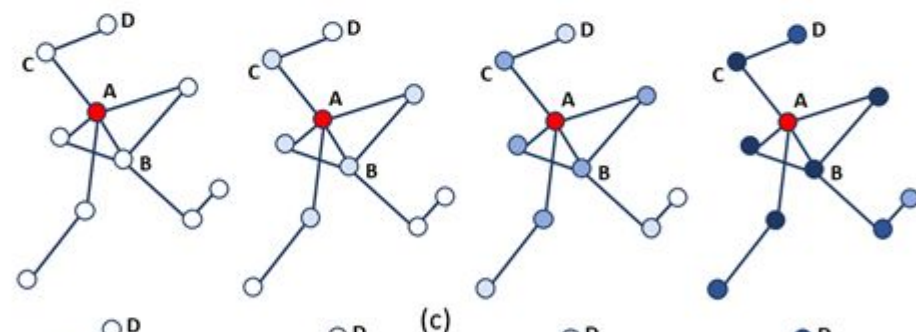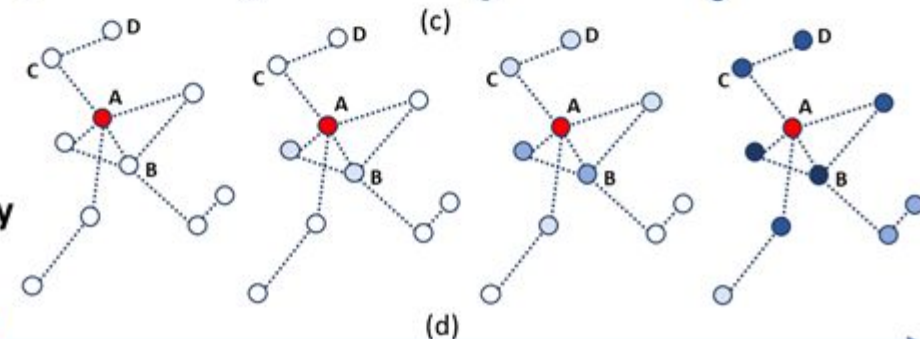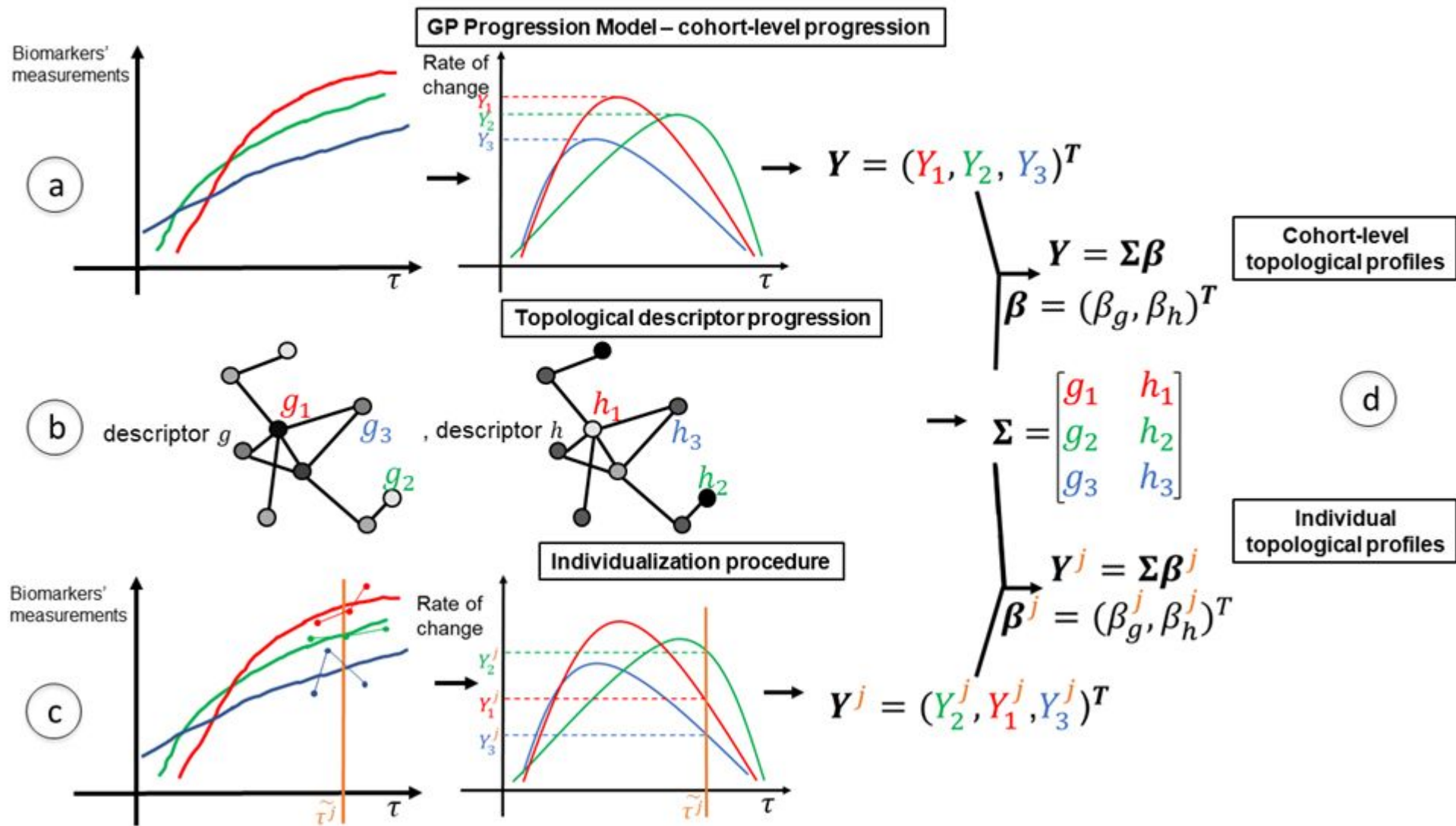
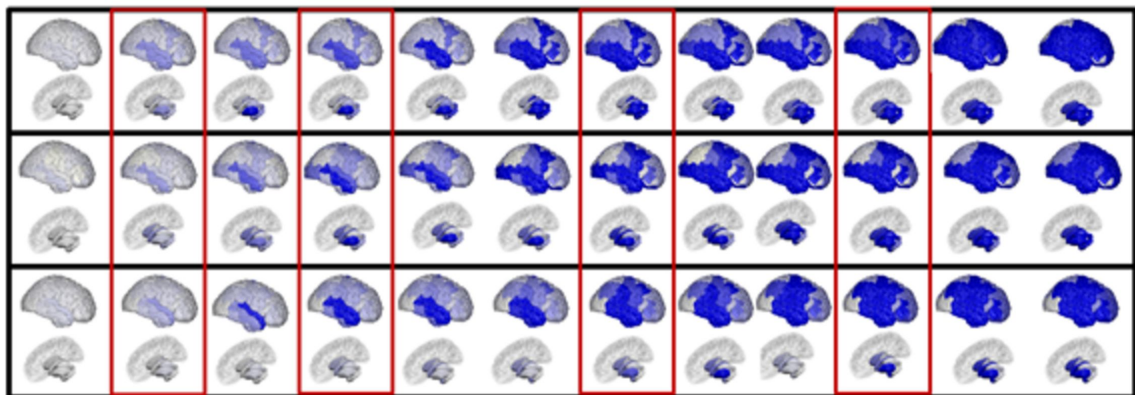# Figure 2–figure supplement 1

AD
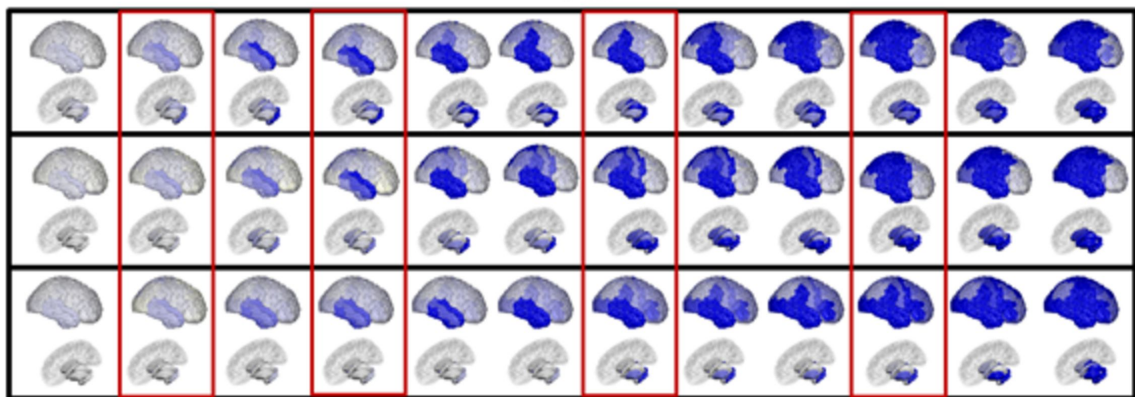
PPMS
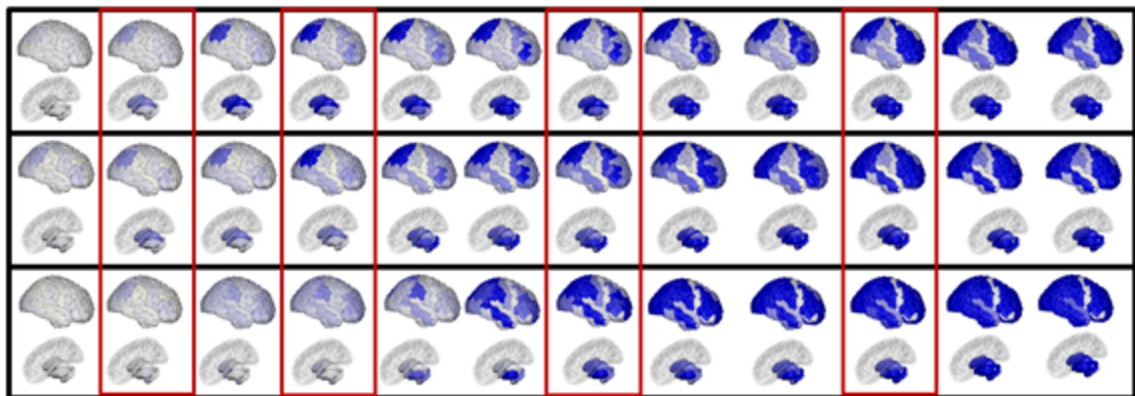
HA

Figure 2–figure supplement 2

Figure 2–figure supplement 3

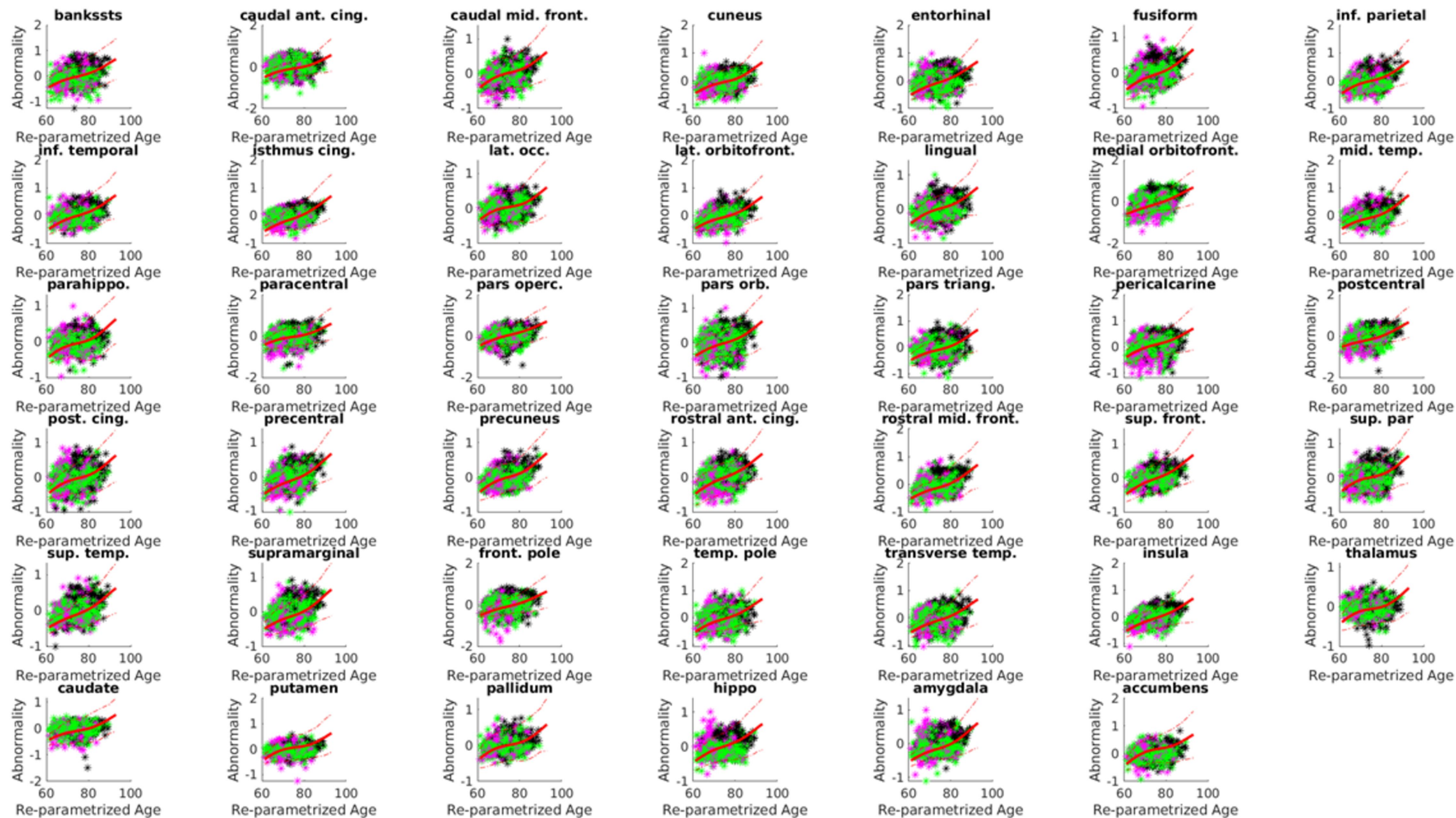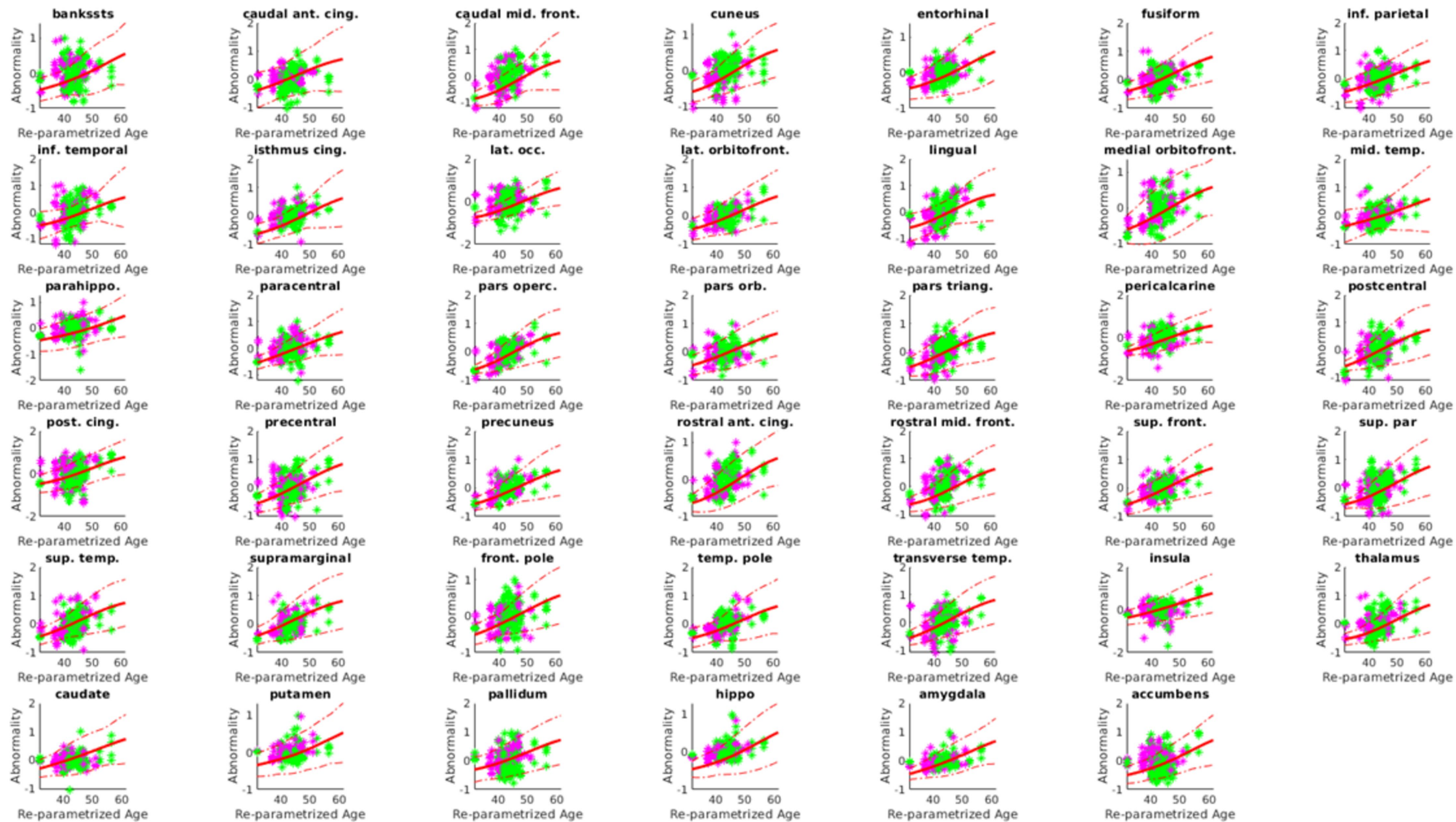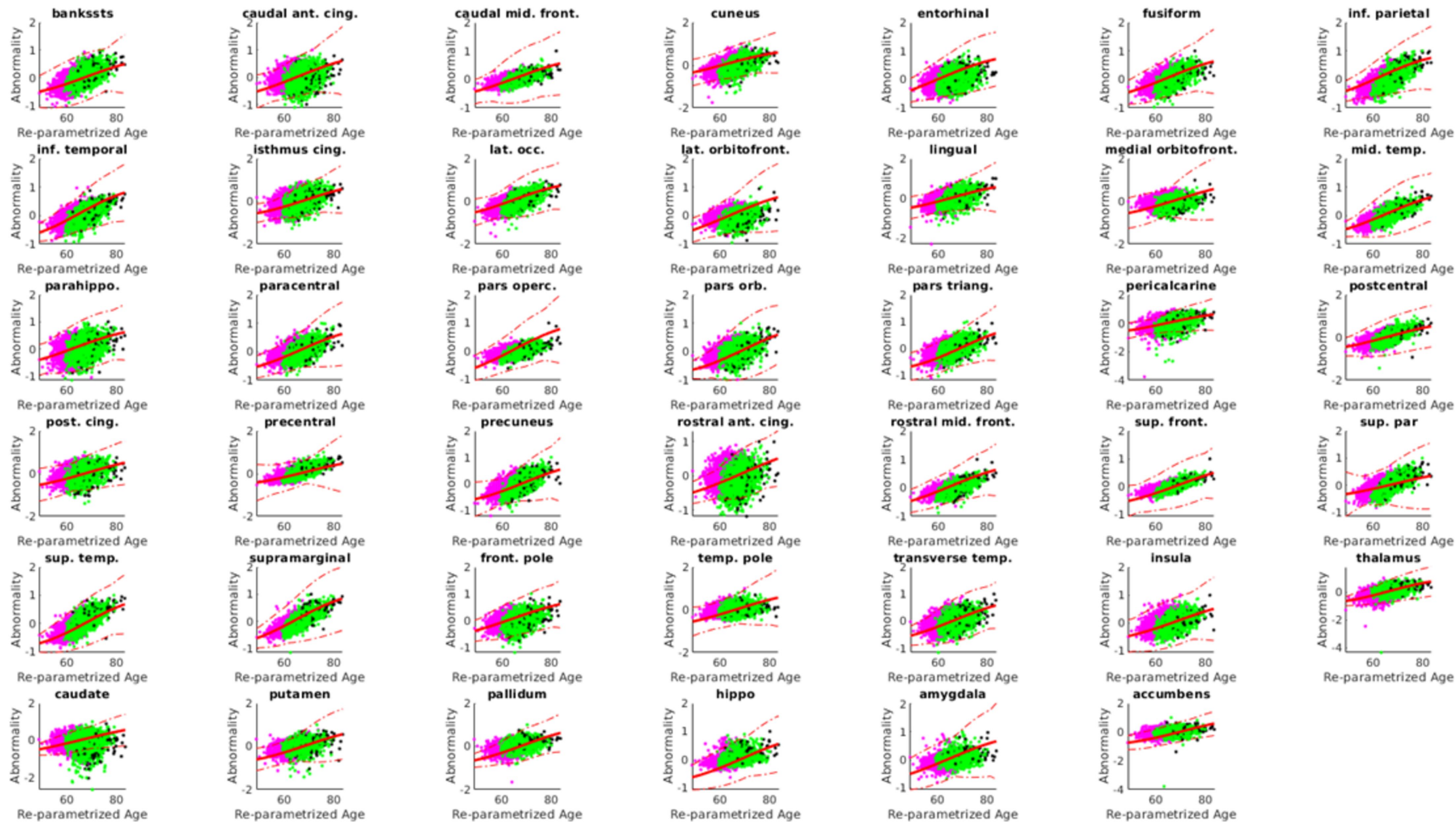# Figure 2–figure supplement 4

Figure 3-figure supplement 1